8-1-2017

NEW INVERSE-HEUSLER MATERIALS WITH POTENTIAL SPINTRONICS APPLICATIONS

Said Bakkar
Southern Illinois University Carbondale, bakkarsaeed@gmail.com

NEW INVERSE-HEUSLER MATERIALS WITH POTENTIAL SPINTRONICS APPLICATIONS

by

Said Adnan Bakkar

B.S., Yarmouk University, 1995
M.S., Al-Albayt University, 2000

A Thesis
Submitted in Partial Fulfillment of the Requirements for the
Master of Science

Department of Physics
in the Graduate School
Southern Illinois University Carbondale
August 2017

THESIS APPROVAL

NEW INVERSE-HEUSLER MATERIALS WITH POTENTIAL SPINTRONICS APPLICATIONS

By

Said Adnan Bakkar

A Thesis Submitted in Partial

Fulfillment of the Requirements for the Degree of Master of Science

in the field of Physics

Approved by:

Dr. Dipanjan Mazumdar, Chair

Dr. Naushad Ali

Dr. Thushari Jayasekera

Graduate School

Southern Illinois University Carbondale

June 26, 2017

AN ABSTRACT OF THE THESIS OF

Said Adnan Bakkar, for the Master of Science degree in Physics, presented on June, 26, 2017, at Southern Illinois University Carbondale.

TITLE: NEW INVERSE-HEUSLER MATERIALS WITH POTENTIAL SPINTRONICS APPLICATIONS

MAJOR PROFESSOR: Dr. Dipanjan Mazumdar

Spintronics or spin-electronics attempt to utilize the electronic spin degree of freedom to make advanced materials and devices for the future. Heusler materials are considered very promising for spintronics applications as many highly spin-polarized materials potentially exist in this family. To accelerate materials discovery and development, The Materials Genome Initiative (https://www.mgi.gov/) was undertaken in 2011 to promote theory-driven search of new materials. In this thesis work, we outline our effort to develop several new materials that are predicted to be 100% spin-polarized (half-metallic) and thermodynamically stable by theory. In particular, two Mn-based Heusler families were investigated: Mn_2CoZ (Z= Ga, Sb, Ge) and Mn_2FeZ (Z=Si,Ge), where the latter is potentially a new Heusler family. These materials were synthesized using the arc-melting technique and their crystal structure was investigated using the X-ray diffraction (XRD) method before and after appropriate annealing of the samples. Preliminary magnetometry measurements are also reported.

We first developed a heat-treatment procedure that could be applied to all the Mn-based compounds mentioned above. Mn_2CoGa was successfully stabilized in the cubic inverse-Heusler phase with a=5.869 Å and magnetic moment of 2.007 μ_B /*fu*. This is in good agreement with prior literature reports [1]. However, cubic phases of

Mn_2CoSb and Mn_2CoGe could not be stabilized within the annealing temperature range that is accessible in our lab.

We successfully synthesized a cubic Mn_2FeSi phase using an annealing procedure similar to Mn_2CoGa. The measured cubic lattice parameter of Mn_2FeSi was 5.682 Å. This is the first experimental report of this material to the best of our knowledge. Detailed analysis of relative intensities of different X-ray peaks revealed that the structure is most likely in an inverse Heusler phase, in agreement with theory. However, a substantial atomic-level disorder was also uncovered from XRD analysis that requires further investigation to understand its effect on its magnetism and half-metallicity. Mn_2FeGe showed the existence of non-cubic phases that substantially weakened at high annealing temperatures.

ACKNOWLEDGMENTS

First of all, I would like to thank my advisor Dr. Dipanjan Mazumdar for his research guidance, his patience, motivation, enthusiasm, and immense knowledge. His wisdom helped me to complete this thesis and increase my research knowledge. Likewise, I would like to thank Dr. Naushad Ali and Dr. Thushari Jayasekera for agreeing to be part of my Master's thesis committee and for their time in providing valuable feedback for the completion of this thesis.

My sincere thanks go to Dr. Ali's group, especially Dr. Igor Dubenko for his supports in the lab and special thanks to Mr. Anil Aryal for involvement in samples' preparation. Also, I would like to thank all the members of the Novel Materials and Heterostructures Laboratory: Mr. Hassana Samassekou, Mrs. Asma Alkabsh, Mr. Yub Raj Sapkota, and Mr. Stephen Hofer for their supports. Furthermore, I would like to thank my friends Mr. Prasanna Patil and Mr. Vishal Balali.

Thanks to the faculties from the Physics department: Dr. Eric Chitambar, Dr. Kuloth Shajesh, and Dr. Leo Silbert for teaching me advanced courses in physics and inspiring me towards research.

Finally, a special thanks to my family: my mother, my wife, my daughter, my brothers and sisters, and my cousin Hussien Albakhit for their support.

DEDICATION

This thesis is proudly dedicated to…

Nihad and Noor

TABLE OF CONTENTS

LIST OF TABLES

TABLE PAGE

LIST OF FIGURES

FIGURE PAGE

CHAPTER 1

INTRODUCTION

There is an increasing demand for new technologies that can help scaling of future electronic devices [3-6]. It is well established for some time now that charge-based devices that rely on materials such as silicon will hit physical limits by 2020 [7]. Out of all the new technologies, spintronics or spin-electronics, a technology that utilizes the electronic spin degree of freedom, is proving to be one of the most viable option to replace or augment charge-based devices [6]. Rapid development of new materials and novel device concepts is proving to be key in this relatively new area [8].

Spintronics technology has already become commercially viable in areas such as magnetic random access memory (MRAM) and hard drive sensors [9,10]. These new devices rely on magnetic materials where spin transport (apart from charge transport) are produced. They are also envisioned to be energy efficient, apart from offering alternative methods to perform logic operations that are essential for high performance computers and smart phones [9,11].

Spintronics started with the discovery of the Giant Magnetoresistance [12], an effect that ultimately led to the 2007 Physics Nobel Prize. The GMR structure consists of alternating multilayer sandwiches of thin nonmagnetic metallic layer (about 1 nm) between two ferromagnetic layers (e.g. Fe/Cr/Fe). Variations of this device prototype make up the read heads in current hard drives. In 1994, it was shown that a nonmagnetic insulating layer will also result in large effect and it is called Tunnel Magnetoresistance TMR device [13,14] or magnetic tunnel junction (MTJ). The GMR and TMR devices show large changes in resistance under the influence of an external

magnetic field (therefore called magnetoresistance or (MR). The magnetic field is required to change the relative magnetic orientation of the ferromagnetic layers. When the magnetizations in the two magnetic layers are parallel, the resistance is low (R_{OFF}) and it becomes high when the magnetization switches to anti-parallel (R_{ON}) as shown in *Fig 1.1*. The magnetoresistance value is defined as the equation

$$MR = \frac{R_{ON} - R_{OFF}}{R_{OFF}} \qquad (1.1)$$

values over 500% (ON/OFF ratio ~ 10) has been recorded at room temperature [14,15].

This idea is used in spin valve devices (see *Fig 1.2*) because we can increase or decrease the flow of the electric current simply by an external magnetic field. Currently, MTJ is the technique employed in nonvolatile magnetic random access memory MRAM. In 1997 IBM designed first GMR hard disk head and in 2005 the commercialization of MTJ started.

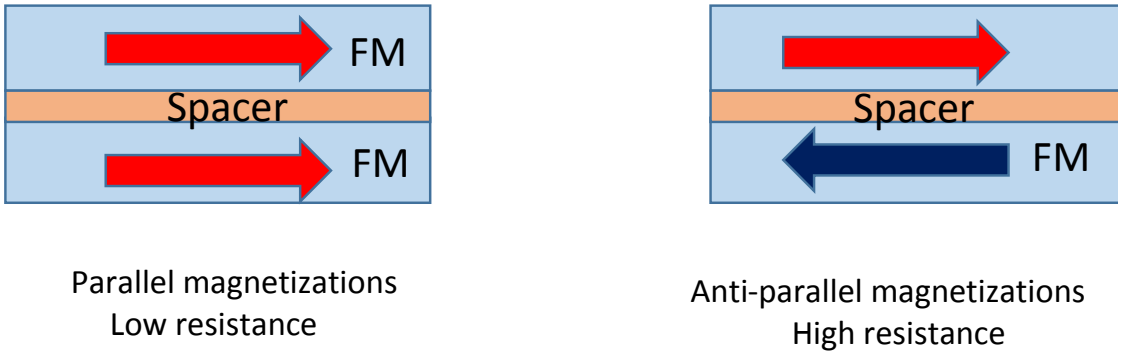

Figure 1.1 Schematic of a typical spintronics device structure. The spacer layer is a non-magnetic metal for GMR and insulator for TMR structures. All layers are of the order of nanometer thickness.

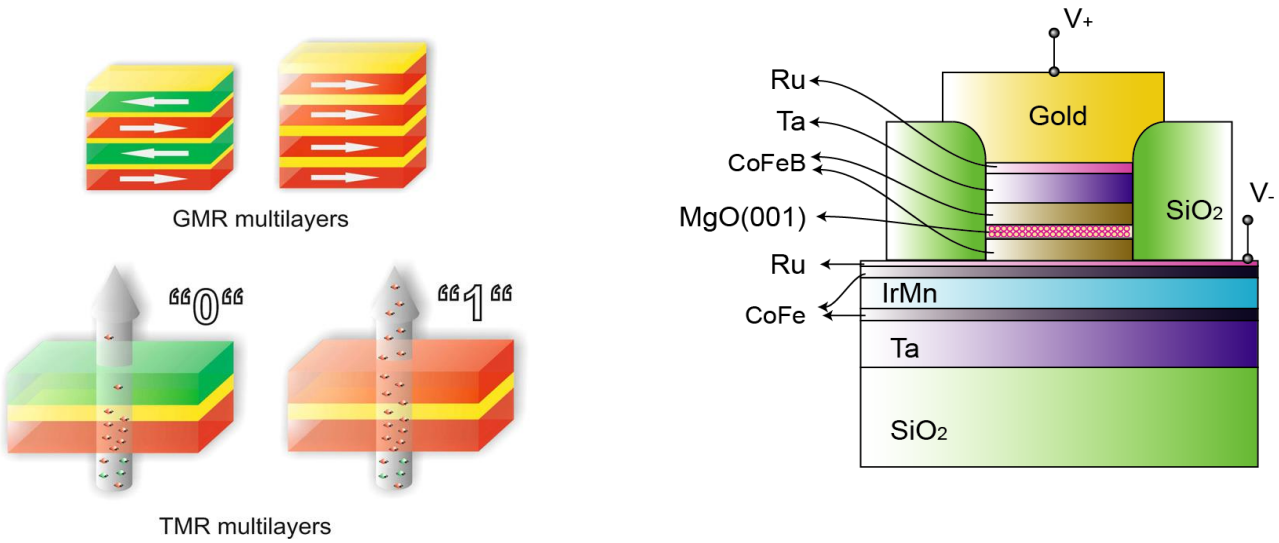

Figure 1.2 Illustration of basic spintronic devices (a) Giant and Tunneling Magnetoresistance devices (GMR) and (TMR) [2], (b) magnetic spin-valve device [16].

1.1 Spin polarization

Spin-polarization is an intrinsic property of any magnetic material. It is quantified by the difference between the number of spin-up and spin-down electrons at the Fermi level.

$$P = \frac{N_{\uparrow}(E_f) - N_{\downarrow}(E_f)}{N_{\uparrow}(E_f) + N_{\downarrow}(E_f)} \qquad (2.1)$$

Where $N_{\uparrow}(E_f)$ and $N_{\downarrow}(E_f)$ represent the density of state of the spin-up and spin-down half bands near the Fermi energy respectively. In non-magnetic materials, the spin-polarization is zero as shown in *Fig 1.3*. But due to the unique band structure of magnetic materials, there is always a net imbalance in the number of spin-up and spin-down electrons.

In 1975, Julliere showed that the magnetoresistance value for TMR devices is related to the spin polarization by the formula [17].

$$TMR = \frac{2P_1P_2}{1 - P_1P_2} \tag{3.1}$$

TMR expresses in terms of the spin polarization of the two ferromagnetic electrodes. This understanding, surprisingly is quite accurate and has survived this day. This formula also provides a clue as to what needs to be addressed for high-performance devices. As P approaches 1, TMR values approaches infinity, which implies that a perfect switch can be made with a 100% spin-polarized material.

However, such materials are not common. The spin-polarization of common ferromagnets such as Fe and Co is about 35-40% [18,19]. It is not only extremely challenging to find such 100% or highly spin-polarized materials (also called half-metals, Fig. 1.3), but to realize high performance spin-valves at room temperature is even harder. Nonetheless the search of high spin-polarized materials is a very vibrant research area in spintronics and is the primary motivation of this thesis work. These materials (half-metals) are the main subject of discussion in this thesis.

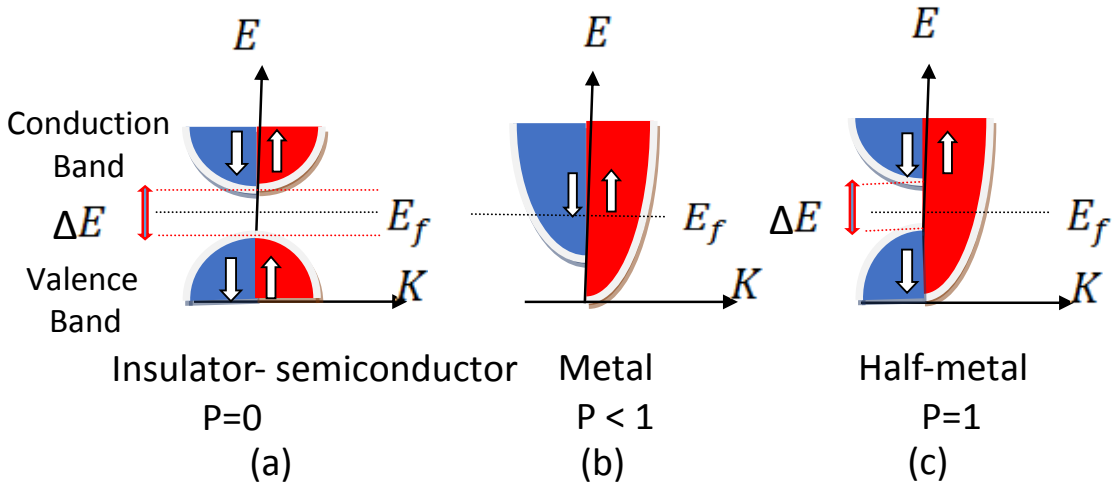

Figure 1.3 Schematic illustration of the spin polarized electronic band structure of (a) insulator or semiconductor (b) metal (c) half-metal where P is the spin polarization as defined by the equation (1.1).

1.2 Half-metals

Half-metals (100% spin-polarized) are ferromagnetic or ferrimagnetic materials with a band gap at Fermi energy for one spin direction. The first compound predicted to be a half-metallic compound was NiMnSb by de Groot and collaborators in 1983 using first-principle calculations [20]. They coined the term half-metal. Half-metallic materials can be thought of as a mixture of a metal (Fig 1.3a) and an insulator (Fig. 1.3b). As shown in Fig. 1.3c, a typical band structure of a half-metal is that of a metallic spin-up channel and an insulating spin-down channel. Simply speaking, there are no electrons with spin-down flavor at the Fermi level ($N_{\downarrow}(E_f)$ =0).Therefore, the Fermi level consists of only a single spin type giving rise to 100% spin-polarization (P=1) as equation (2.1) [21,22]. *Fig. 1.4* is shown the density of states of real materials that are considered half-metallic Co_2TiGe [23].

Experimentally, half-metals have been found in (a) Perovskite or double Perovskite oxides as Sr_2FeMoO_6 [24], (b) transition metal oxides as CrO_2 [25], Fe_3O_4 [26] or the colossal magnetoresistance material $La_{0.7}Sr_{0.3}MnO_3$ [27] using either Andreev reflection or spin-polarized tunneling spectroscopy. The experimental case of Heuslers has been controversial to some extent as they are prone to structural disorder which disrupts the half-metallic character. On the other hand, large room temperature TMR effect has been observed in Heusler based devices that is only consistent with high spin-polarization [13,14]. In contrast, oxide half metals ferromagnets work only at low temperatures as they have low Curie temperature [28,29]. Therefore, the strong motivation to study half-metals is to use it in spintronic applications [22], spin filters [30], spin injection devices [31] giant magnetoresistance (GMR) [12,32], colossal magnetoresistance (CMR), and tunneling magnetoresistance (TMR) devices [13].

It was found that the spin polarization (half-metallicity) is influenced with the atomic disorder [33]. Therefore, the higher spin polarization can be achieved with a higher degree of order of the atomic structure [34]. Recently, ternary Heusler compounds (general formula X_2YZ or XYZ) with high atomic order have been identified as one of the promising materials family to realize 100% spin-polarized materials. Coupled with high spin-polarization, they also show extremely high magnetic Curie temperature (~500-1000K) making them technologically viable for applications. In this thesis, a new set of potential half-metallic materials in this family, as identified by theory, was developed.

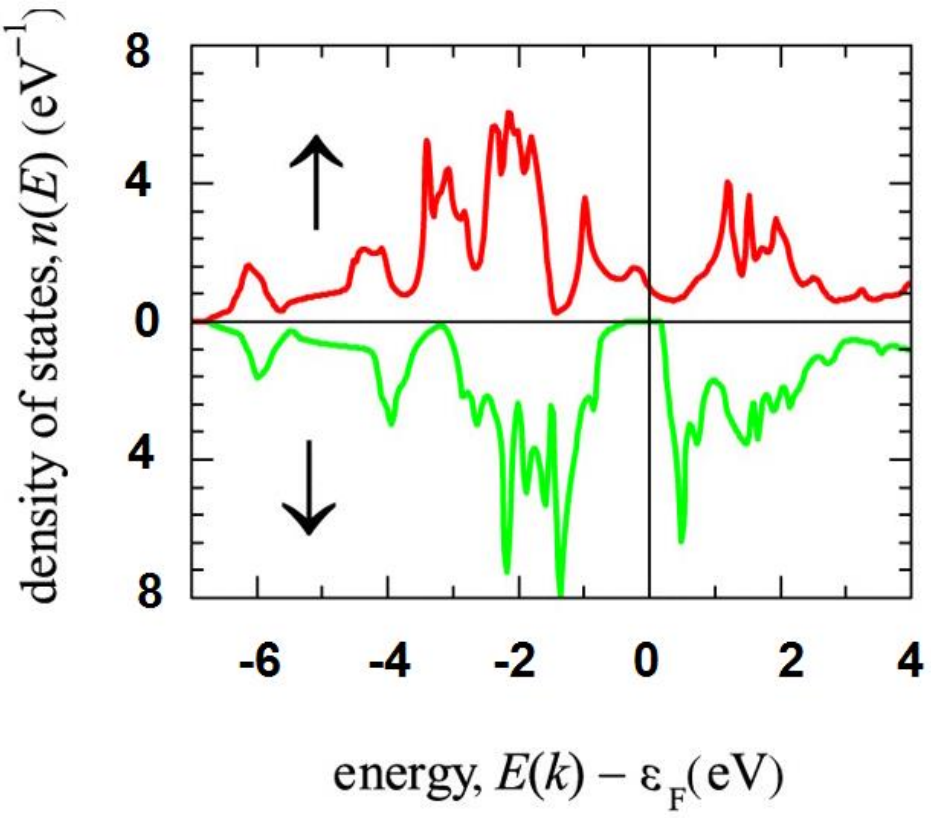

Figure 1.4 Electronic structure of Co_2TiGe showing the density of states [23].

1.3 Thesis statement

In this work, we have fabricated and investigated a number of potentially new half-metallic Manganese-based inverse Heusler alloys. Specifically, most of this work focused on stabilizing and investigating the crystal structure of a few arc-melted Heuslers of the type Mn_2CoZ (Z= Ga, Ge, Sb) and Mn_2FeZ (Z= Si, Ge). The chosen materials were guided by first-principles theory calculations in the framework of the DMREF initiative whereby promising stable half-metallic materials was identified [35]. During this thesis work, we have identified one new Heusler compound that has not been experimentally reported before to the best of our knowledge.

1.4 Thesis Outline

In chapter 2, the structure-property relationship of Heusler alloys, and other necessary theoretical background is discussed. Chapter 3 discusses the experimental techniques employed in this work. In chapter 4, the experimental results data are discussed in details. Finally, chapter 5 presents the conclusion of this study.

CHAPTER 2

THEORETICAL BACKGROUND

In this chapter, we discuss the theoretical background of this thesis. In section 2.1, we explore the structure-property relationships of Heusler compounds. Next, we discuss the methods we employ to characterize their structural and magnetic properties, namely X-ray diffraction and magnetometry. In the last section of this chapter, we shall review the literature.

2.1 Heusler compounds

In 1903 [36,37], Friedrich Heusler discovered a series of ferromagnetic alloys composed of diamagnetic and paramagnetic elements that are considered nonmagnetic such as Cu_2MnAl. More than 1500 compounds are known now, and called Heusler compounds. Many are predicted theoretically to be half-metals. In addition to the metallic and half-metallic compounds this family includes semiconducting, superconducting, and topological insulator materials [38,39].

There are two types of Heusler compounds: half Heusler compounds and full Heusler compounds. Half Heusler materials are ternary intermetallic compounds with composition XYZ, where X and Y atoms have cationic character, whereas Z atom could be the anionic element. The X and Y atoms represent transition metals or rear earth elements. While, the Z atom represents the main group element from the second half of the periodic table as it is shown in *Fig. 2.1*[2]. Similarly, the Full Heusler materials are ternary intermetallic compounds with composition X_2YZ. see *Fig. 2.1*. We are particularly interested in Full Heusler compounds as their electronic properties depend on the precise nature of atomic-level ordering.

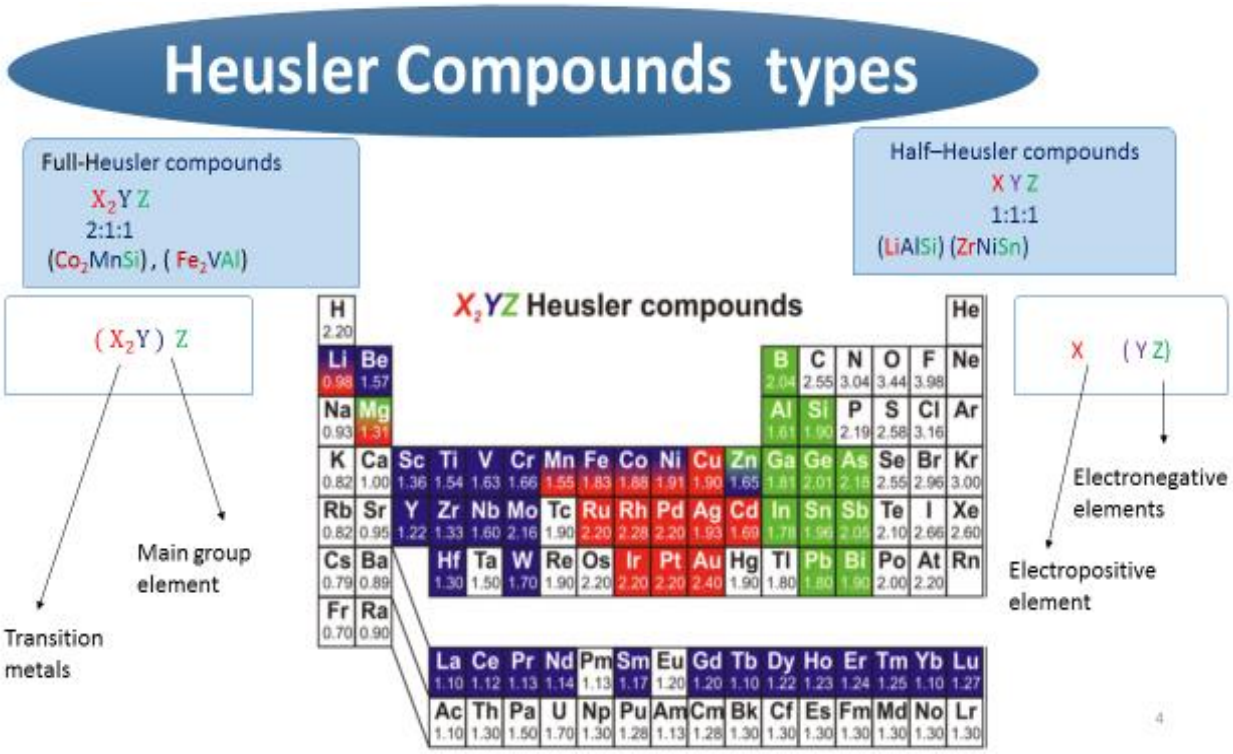

Figure 2.1 The periodic table of elements with different colors to explains the types of Heusler materials formula [2].

2.1.1 Crystal Structure of Heusler alloys

In general, Heusler compounds are divided into two types; regular types (X_2YZ or XYZ) and Inverse types (XYX'Z). The half Heusler alloys with high order usually follow the $C1_b$ structure as shown in *Fig 2.2a,* while the full Heusler alloys follow the $L2_1$ structure as shown in *Fig 2.2b.* As mentioned earlier, the X and Y atoms in the stoichiometric composition X_2YZ and XYZ of Heusler alloys represent different transition metals, but the Z atoms represent either non-magnetic [20] metals or semiconductors [40]. Hence, the $L2_1$ structure with cubic Cu_2MnAl as a prototype has a unit cell with four face centered cubic (*fcc)* sub-lattices and belongs to the space group $Fm\bar{3}m$ (225). The Wyckoff coordinates are Cu at 4a (0,0,0), and at 4b (1/2,1/2,1/2) ,Mn at 8c (1/4,1/4,1/4), and Al at 4d (3/4,3/4,3/4).

The inverse Heusler alloys (XA) is obtained by switching positions of one atom of X atoms with a Y atom and typically follows the $CuHg_2Ti$ type in space group $F\bar{4}3m$ (216) as shown in *Fig 2.2c.* The standard $Fm\bar{3}m$ cell structure of X,X,Y,Z is formed at the positions (0,0,0), (1/2,1/2,1/2), (1/4,1/4,1/4) and (3/4,3/4,3/4) respectively Fig *2.2.* Whether a full Heusler adopts an L21 or XA structure depends on the number of valence electrons. Inverse Heusler alloys are observed when the atomic number of the Y atom is higher than that of X from the same period, which means that the number of 3d valence electrons of Y atoms is greater than that of X [41].

The $L2_1$ and XA structures are considered 100% ordered. But when there are disorders in the Y and Z sites (for instance exchange of Y and Z atom), they become disorder alloys and adopt a B2 structure see *Fig 2.2 d.* In addition, even a higher disordered structure (A2) is possible. In this phase, there are disorders in all sites and

X, Y, Z atoms are randomly distributed with no preference, i.e. both X and YZ sub-lattices are disorder as shown in *Fig 2.2e*. As we shall explain below, X-ray diffraction can pick up evidence of all such phases.

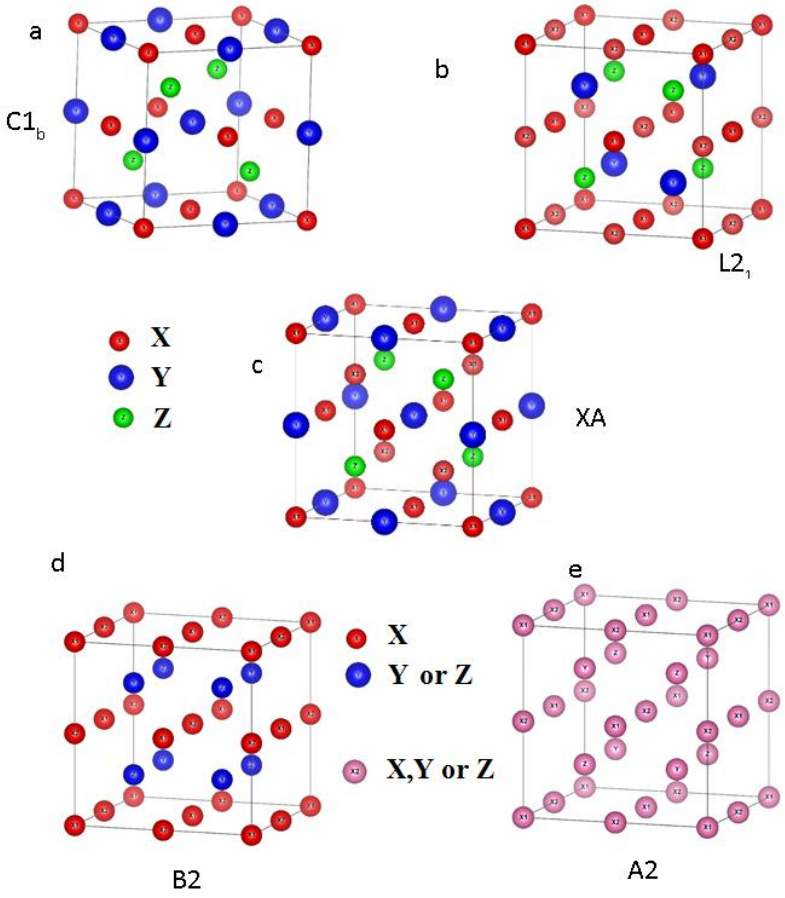

Figure 2.2 Schematic representations of (a) Half Heusler structure C1b, (b) Full Heusler Structure L21, (c) Inverse Heusler structure XA, (d) B2 Structure, and (e) A2 structure.

2.2 X-ray Diffraction for Determination of Crystal Structure

To investigate the crystal structure and phase of solid state systems, usually we use the X-ray diffraction (XRD) technique. When X-rays are incident on a crystalline solid, it will be scattered from the crystal lattice and the peaks intensities of scattered X-rays are typically recorded under the specular condition (the incident angle is equal to the scattered angle). Also, when the path length difference equals $n\lambda$ will results in a constructive interference where n is an integer number and λ is the X-ray wavelength.

In the case of crystalline solid, the lattice planes are separated by the interplanar distance *d* see *Fig 2.5*. If two waves are scattered from lattice planes and interfere constructively, then the path difference between the two waves is given by $2d\sin\theta$ where θ is the scattering angle which follows Bragg's law

$$n\lambda = 2d\sin\theta \tag{2.1}$$

Bragg's law explains the interference pattern of X-ray scattered by the crystals and the X-ray diffraction pattern (XRD) contains the peaks at specific angles.

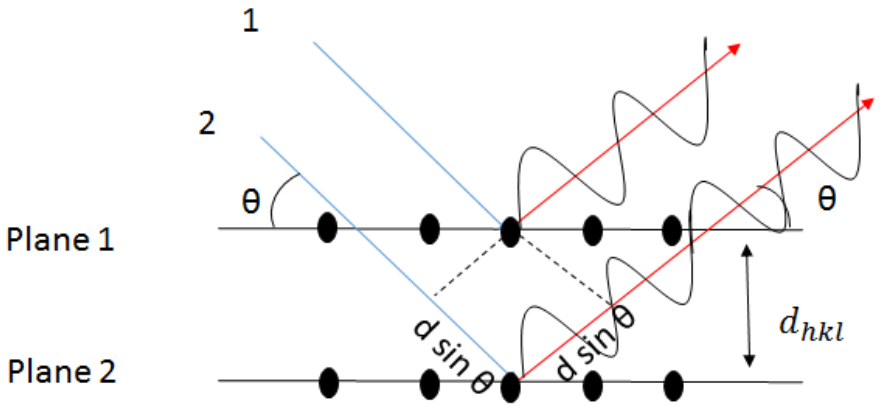

Figure 2.3 Bragg diffraction for two identical beams in wavelengths and phase are scattered from two atoms in different planes.

By analyzing the XRD pattern we can identify the crystal structure and phase. The positions of diffraction peaks in the XRD pattern are used to find the shape and size of the unit cell, while the relative intensities of diffraction peaks are used to determine the atomic position. We use the Miller indices (hkl) to index the lattice planes, so for different crystal structure, the relations between the interplanar distance $d_{(hkl)}$ and the lattice parameters *(a,b,c)* are given by the following plane spacing equations :

Cubic $$\frac{1}{d^2} = \frac{h^2 + k^2 + l^2}{a^2} \quad (2.2)$$

Tetragonal $$\frac{1}{d^2} = \frac{h^2 + k^2}{a^2} + \frac{l^2}{c^2} \quad (2.3)$$

Hexagonal $$\frac{1}{d^2} = \frac{4}{3}\left(\frac{h^2 + hk + k^2}{a^2}\right) + \frac{l^2}{c^2} \quad (2.4)$$

Orthorhombic $$\frac{1}{d^2} = \frac{h^2}{a^2} + \frac{k^2}{b^2}\frac{l^2}{c^2} \quad (2.5)$$

2.2.1 Structure Factor (*F)*

Atomic arrangement within crystals also affect the X-ray intensities apart from lattice spacing. This is captured in the structure factor. It represents the resultant wave scattered by the atoms of unit cell in the crystal. To obtain the structure factor, we should add together all the waves scattered by the individual atoms and it is given by the equation:

$$F_{hkl} = \sum_{1}^{N} f_n e^{2\pi i(hu_n + kv_n + lw_n)} \tag{2.8}$$

Where, $u \;\; v \;\; w$ are the coordinates of the atom and the summation extends over all *N* atoms of the unit cell and f is the atomic scattering factor. The scattered intensity by all atoms of unit cell is proportional to $|F|^2$ [42].

2.2.2 X-ray diffraction pattern for the order and disorder Heusler compounds

We shall utilize the structure factor dependence to investigate the atomic-level structure of Heuslers. Theoretical studies [33,43] show that atomic distribution within the Heusler unit cell strongly affect their electronic structure, magnetic and transport properties. For instance, it is also now well know that anti-site disorder can destroy the half metallicity [44]. Their X-ray diffraction can be a valuable method in interpreting such situations. Let us explain how in some details.

The $L2_1$ and XA structure have the highest atomic order in full-Heusler alloys. In contrast, the A2 structure is the lowest one and considered the fully disordered atomic structure within the Heusler family, while, the B2 structure is partially disordered. Ordering results in bigger unit cells. Therefore, $L2_1$ alloys (X_2YZ) consist of eight stacked (*bcc*) sub-lattices where, X atoms are site on the corners while Y and Z atoms are occupied the center of the (*bcc)* lattices regularly.

The XRD patterns of full Heuslers can divided into three different types [45]. First, the odd super-lattice peaks where (hkl) are odd numbers (e.g. (111)) is found only in the $L2_1$ or XA structure, see *Fig*. 2.4(c)*.* The second type of even peaks are observed when h+k+l=4n+2, e.g. (200). Such peaks are observed in both ($L2_1$) and (B2) structures as

shown in *Fig 2.4(b)*. Finally, the fundamental diffraction type which appears in case h+k+l=4n e.g. (220) and these diffractions are observed in the all structure types, even for highest disorder A2 structure (Fig. 2.4(a)). The structure factors of the $L2_1$, XA, B2, and A2 phases are shown in the Table 2.1. and the low index structure factors are shown in Table 2.2 .

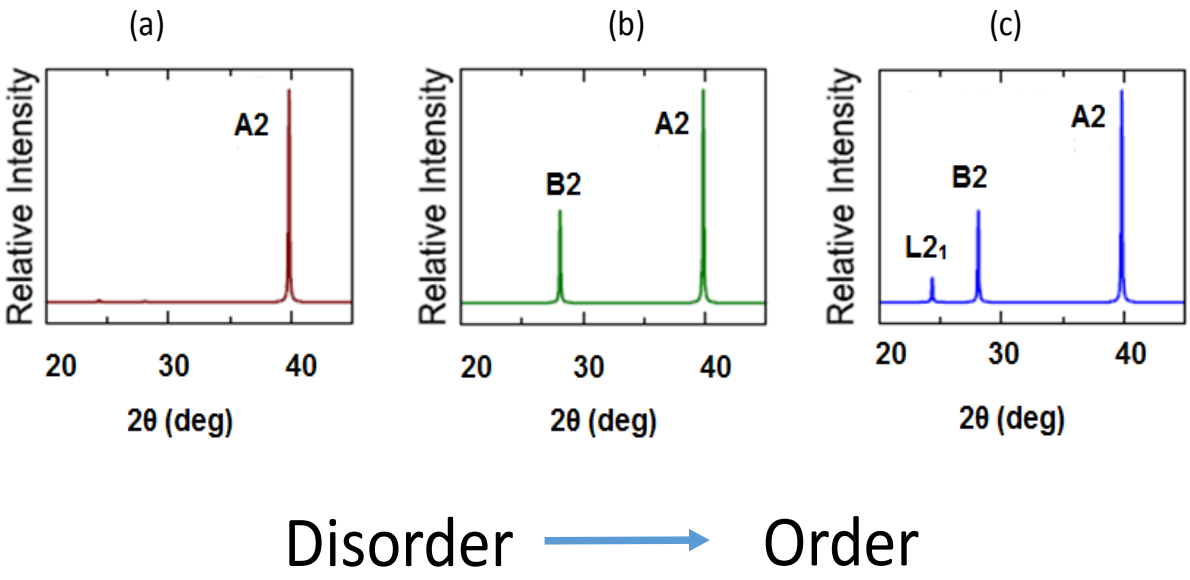

Figure 2.4 Illustration of simulated XRD patterns in different types of crystal structures from disorder to order: a) A2 type, b) B2 type, c) $L2_1$ type.

Table 2.1: The structure factors for the ideal ($L2_1$, Xa, B2, and A2) phases.

Structure Phase	Structure factor (*F*)	(*hkl*) value
$L2_1$	$F = f_z + f_y + 2f_x$	(*hkl*) even, *h+k+l=4n*
	$F = f_z + f_y - 2f_x$	(*hkl*) even, *h+k+l=4n+2*
	$F = f_z - f_y$	(*hkl*) odd
XA	$F = f_z + f_y + 2f_x$	(*hkl*) even, *h+k+l=4n*
	$F = f_z - f_y$	(*hkl*) even, *h+k+l=4n+2*
	$F = f_z - (1+i)f_x + if_y$	(*hkl*) odd, *h+k+l=4n+1*
	$F = f_z - (1-i)f_x - if_y$	(*hkl*) odd, *h+k+l=4n+3*
B2	$F = f_z + f_y + 2f_x$	(*hkl*) even, *h+k+l=4n*
	$F = f_z + f_y - 2f_x$	(*hkl*) even, *h+k+l=4n+2*
A2	$F = f_z + f_y + 2f_x$	(*hkl*) even, *h+k+l=4n+2*

Table 2.2: The low index structure factor for ($L2_1$ and XA) phases.

(*hkl*)	Structure factor (*F*) of $L2_1$	Structure factor (*F*) of XA
(111)	$F = f_z - f_y$	$F = f_z - (1-i)f_x - if_y$
(200)	$F = f_z + f_y - 2f_x$	$F = f_z - f_y$
(220)	$F = f_z + f_y + 2f_x$	$F = f_z + f_y + 2f_x$

2.3 Magnetism and magnetic properties of Heusler compounds

In 1820 Oersted discovered that magnetic field is generated when electric current is passed through a conducting wire. Magnetization is defined as magnetic moment per unit volume $\vec{M} = \sum \vec{\mu} / V$ *(emu/cm³)* [46].

The motion of electrons results in an orbital magnetic moment ($\vec{\mu}_{orbit}$). Intrinsically, electron also possess the spin magnetic moment ($\vec{\mu}_{spin}$). The total magnetic moment of an atom is $\mu = -gJ\mu_B$ where ***J*** is the total sum of total orbital and spin angular momentum, g is the Lande-g factor (g -factor) and for an electron is g =2 and μ_B is the Bohr magneton and is given by

$$\mu_B = \frac{e\hbar}{2m} \tag{2.9}$$

Depending on the internal arrangement of these moments, magnetic materials are divided into five different types: Diamagnetic, Paramagnetic, Ferromagnetic, Anti-ferromagnetic, and Ferrimagnetic materials.

The magnetic properties of Heusler compounds depend on their atoms sites, particularly the X atom site. Half- Heusler compounds XYZ have only one magnetic moment sub-lattice from the atoms on the octahedral sites. On the other hand, the full-Heusler compounds X_2YZ have two magnetic moment in the octahedral sites, which causes ferromagnetic or anti-ferromagnetic coupling as shown in *Fig. 2.5.*

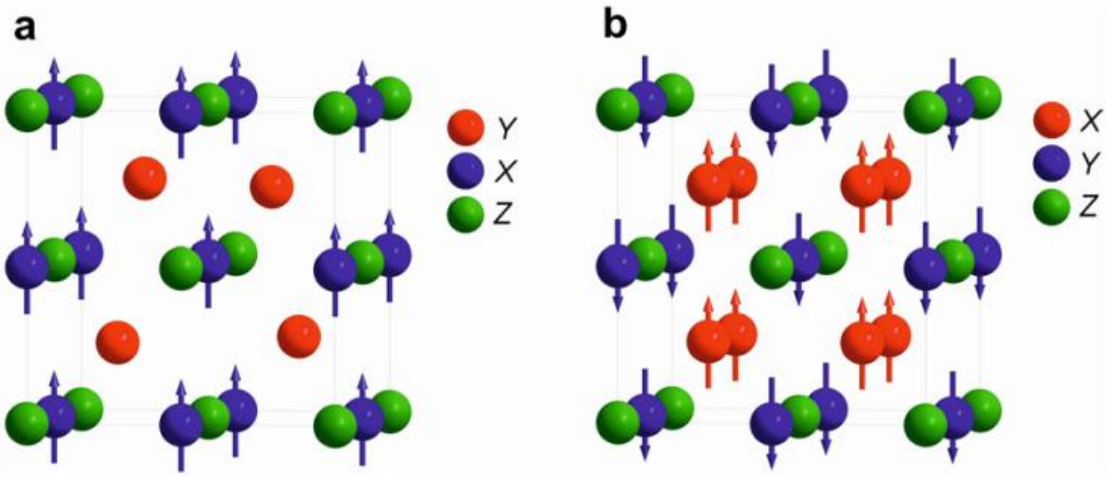

Figure 2.5 The magnetic moment for (a) Half Heusler compounds XYZ, (b) Full Heusler compounds X_2YZ [2]

According to Slater and Pauling, the average valence electron number N_v per atom can be the basis of estimating the magnetic moment of the 3d elements and binary alloys [47,48]. Also, depending on the Slater-Pauling curve, which shows the areas of low and high valence electron concentration, it was found that the Heusler compounds are set in the area with low valence electron N_v and localized magnetism related to the *bcc* structure. The magnetic moment in multiples of Bohr magnetons is given by $m = N_V - 2n_\downarrow$, where $2n_\downarrow$ is the number of electrons in the minority states. Because of the electron in the d minority band is approximately 3 electrons, the magnetic moment per atom is $m \approx N_V - 6$. Therefore, the half Heusler compounds have 3 atoms the magnetic moment is $m = N_V - 18$ and for full Heusler compounds which consist of four atoms the magnetic moment is given by $m = N_V - 24$. *Fig 2.6*

shows the Slater-Pauling curve for examples of Mn-based and Co-based compounds [49].

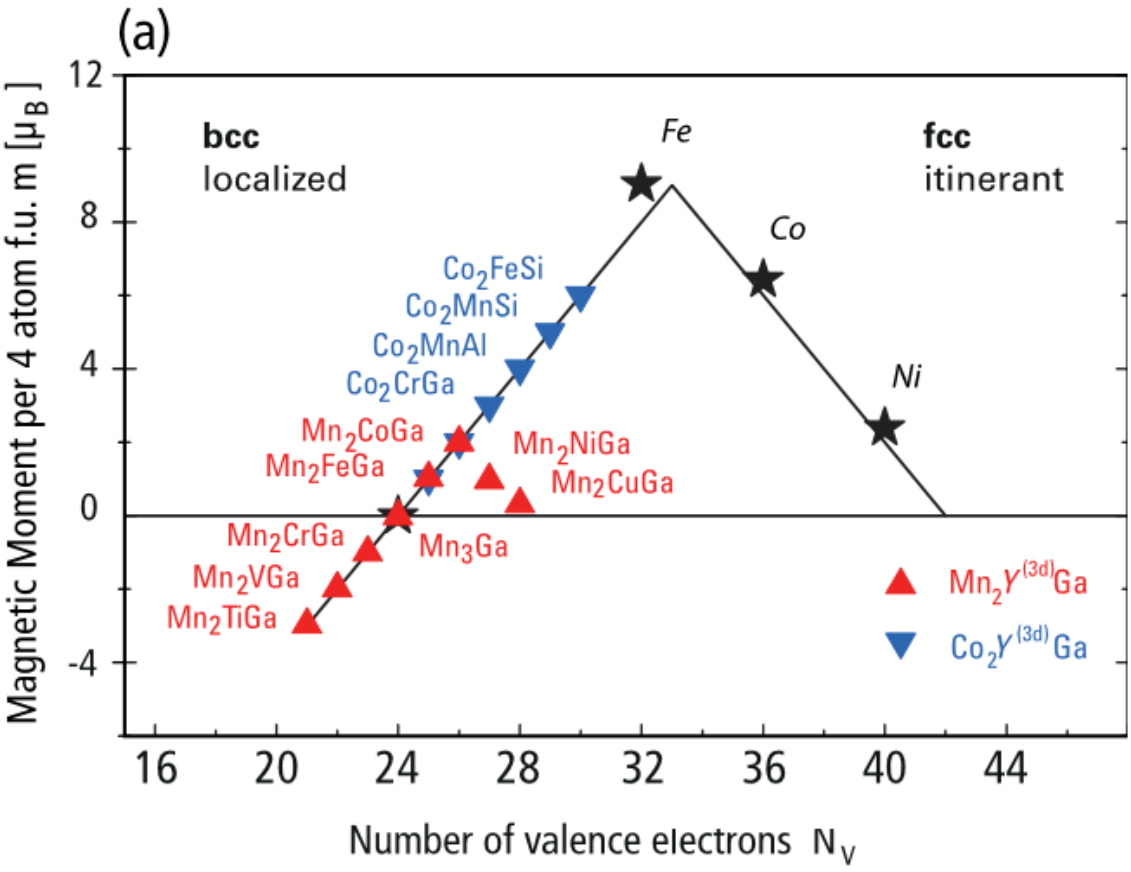

Figure 2.6 Slater-Pauling curve for $Mn_2Y^{(3d)}Ga$ and $Co_2Y^{(3d)}Ga$ compounds [49].

2.4 Literature review

The Co_2YZ and Mn_2YZ families constitute the majority of the expected half-metallic Heusler alloys. It was found that the Y atoms with low or high valence electrons couldn't affect the properties of half-metallic alloys of Mn_2YZ such as V or Co respectively [50,51] whereas Mn atoms strongly influence the formation of half metallicity. Mn_2VAl has been studied theoretically as the first half-metallic ferromagnet [50]. Then Mn_2CrAl and Mn_2CrSb were predicted as a half-metallic antiferromagnets in Heusler alloys [52], also the Mn_2CoSb is reported as a half-metallic ferromagnet [51], and Sabine Wurmehl and et.al. found in their theoretical study that according to Slater–Pauling rule, the half-metallic system of interest must have 24 valence electrons such as Mn3Ga [53].

Many newer half-metallic full Heusler compounds are predicted from ab-initio calculations but may or may not be experimentally realizable. In this work, we shall investigate inverse Heusler compounds of two Mn-based families; Mn_2CoZ (Z= Ga, Ge, Sb) and Mn_2FeZ (Z= Si, Ge) which are predicted to be half-metallic alloy [35,54].To achieve viable practical application, two stringent criteria must be met. First condition that is the material must be experimentally proven to be 100% spin polarization at fermi level and the second condition is that it should have a high Curie temperature. In this work, we shall only explore the feasibility of growing these materials in bulk form, and not address the harder studies of spin-polarization. Our material choices are exclusively based on theoretical predictions of half-metallicity in 100% ordered Heusler structures at zero temperature using density functional theory.

Recently, theoretical studies have been conducted on these alloys. Yuepeng Xin et al. [55] conducted a competition study on these alloys and found that they are stable as half-metals. In addition, another theoretical study [56] using the *ab-initio* band structure calculations show that all Mn_2CoZ materials are ferrimagnetic except Mn_2CoSb which is a ferromagnetic alloy. Also, in this study the Curie temperature was calculated for Mn_2CoZ (Z= Ga, Ge, Sb) using mean field approximation methods and the reported values are 886, 579, 567 K respectively. This study shows that the Curie temperature decreases with increase in total valence electrons number (N_v)

Experimentally, Mn_2CoGa [57] has been successfully grown in a cubic Heusler phase with a high Curie temperature. Furthermore, G. D. Liu *et al.* reported growth of many Mn_2CoZ (Z= Ga, Ge, Sb, Al, In, Sn) compounds [54]. They confirmed that the electronic structure and magnetic properties of this family follows the Hg_2CuTi type (XA) and not $L2_1$ structure for the spin-up (majority) and the spin-down (minority) electrons, and they theoretically reported that all the compounds are half-metal ferrimagnet.

In contrast, K. Minakuchi et al. [58] and R. Y. Umetsu et al. [59] found experimentally that the crystal structure of the Mn_2CoGa is $L2_{1b}$ type with space group $Fm\bar{3}m$ number (225) and not Hg_2CuTi type with space group *F-43m* number (216).

So far, Mn_2FeZ (Z= Si, Ge, Ga, Sb, Al) compounds are reported only theoretically. Luo et al. found that the Mn_2FeGe and Mn_2FeSi are not half-metal at equilibrium lattice constant and they attribute that to the lattice constant size. An expansion of the lattice can decrease the minority gap width [60]. They also calculated the total magnetic moment for the Mn_2FeGe and Mn_2FeSi and found it to be 2 μ_B/f.u.

Figure 2.7 Electronic structure of Mn_2FeSi shown the density of states [35].

However, latest theoretical work by the University of Virginia and Northwestern University team [35], reported that Mn_2FeGe and Mn_2FeSi are stable half-metallic ferromagnets in the inverse-heusler structure with a lattice constant of 5.72 Å and 5.6006 Å respectively as shown in *Fig 2.7*. Encouraged by these predictions we show our results on such materials next.

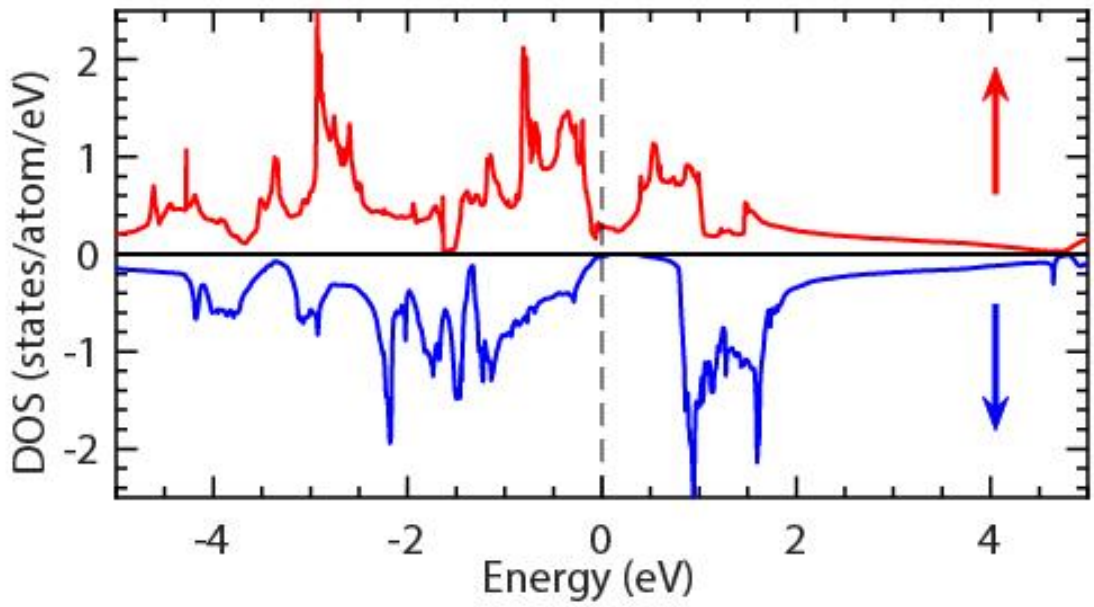

Figure 2.7 Electronic structure of Mn_2FeSi showing the density of states [35].

CHAPTER 3

EXPERIMENTAL TECHNIQUES

In this chapter, many different experimental techniques for our research work are discussed. The experimental techniques involve sample preparation, room temperature X-ray diffraction (XRD), metallography, and magnetization measurement.

3.1 Sample preparation

The bulk off-stoichiometric polycrystalline samples (3 g) of the two Heusler families Mn_2CoZ (Z= Ga, Ge, Sb) and Mn_2FeZ (Z= Si, Ge) were prepared by arc-melting which constituent elements of purity better than 99.99% under the constant flow of "ultra-high" purity argon using water-cooled massive bronze crucible and tungsten electrode see *Fig 3.1.* Each sample was re-melted three to four times for homogeneity. 3% excess Mn was added in advance to compensate for the fact that Mn is volatile. The loss of elements during melting was monitored by measuring the total sample mass using an analytical balance with an accuracy of 5×10^{-5} g. Finally, the homogenous samples were cut into many pieces for the annealing process.

Two different methods were used to anneal the samples. Some samples were wrapped in tantalum foils and annealed in high vacuum (~10^{-5} torr) inside quartz tube. Other samples were annealed in encapsulated vacuum quartz tubes. The annealing temperatures and heat-treatment time duration were changed to achieve the best conditions. The Mn_2CoZ (Z= Ga, Ge, Sb) samples were annealed at 500 C^0, 700 C^0 and 900 C^0 for 2 days, while the Mn_2FeGe was annealed for 2 days at 500C^0 and 900 C^0 and the Mn_2FeSi was annealed at 500 C^0 for 2, 5 and 10 days to study the degree of

ordering. Finally, the samples were cooled slowly to room temperature after annealing for determining their crystal structure by using the X-ray diffractometry.

Figure 3.1 The arc-melting system.

3.2 X-ray diffraction measurements

X-ray diffraction measurements were performed to determine their crystal structure. the XRD measurements were done by using the Rigaku SmartLab X-ray diffractometer model (2080B411) designed by Rigaku Corporation as shown in *Fig 3.2.*

The sample preparation of the samples for the XRD measurement consisted of two steps. First, the small pieces of the annealed specimen are crushed into powder by using a mortar and pestle in an alcohol (isopropanol) solution to prevent the sample from oxidation. It is well known that reducing the particle size and increasing the number of particles will help to get a perfect powder diffraction pattern. Second, the powder was spread uniformly over a flat plate that is designed to reduce the XRD background. All samples were measured in a (θ - 2θ) mode with *Cu Kα* radiation (1.541 Å) and parallel beam (PB) geometry. The XRD diffractometer consists of an X-ray tube with voltage-current rate (20-45 KV, 10-200 mA) and intensity detector scintillation counter D/teX ultra/ diffracted beam monochromator for *Cu*. The X-ray generator is cooled by a water cooling system. The XRD scans were performed in the 2θ range of 20° - 90° with step size 0.02 degree and speed 0.1°/min at room temperature using the *Kβ* filter. The data was recorded by automated computer software of SmartLab Guidance and the basic data processing was performed by the PDXL program.

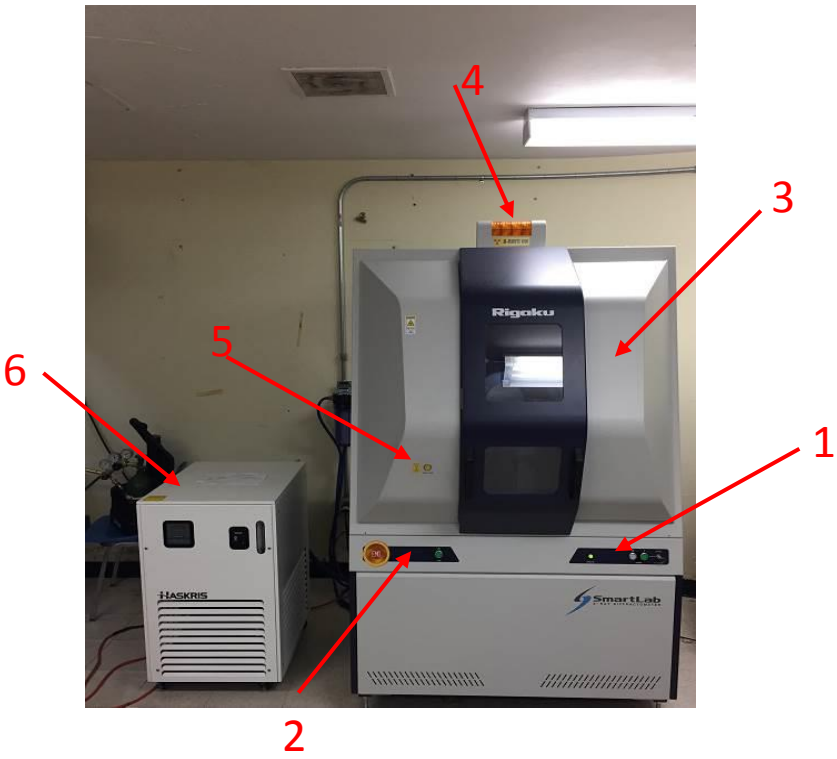

1. Main panel	**Panel used to start and stop SmartLab**
2. Operating panel	**Panel used to turn the internal light on/off**
3. Door	**This door is opened to change samples and optical devices**
4. X-ray warming lamp	**Light when X-rays are generated**
5. Door-lock button	**Lock/Unlock the door**
6. Cooling system	**X-ray generator water cooling unit**

Figure 3.2 Front view of SmartLab X-ray diffractometer designed by Rigaku Corporation.

3.3 Metallography

The microstructural observation is a direct method to judge and determine the optimal promising equilibrium conditions such as the annealing time and temperature. However, the specimens need to be polished and etched to expose the crystal grains. First, the annealed pieces are rough-polished using three different SiC paper (sandpapers) from rough 150, 220 to smooth 600 using a turntable machine or manually. Secondly, a final polishing step is performed on the specimen with diamond paste. To see the crystals' grains and grain boundaries, the specimen must be etched. Therefore, the third step is etching the sample using Marble's reagent for 30 seconds and then rinsing it thoroughly with water and alcohol and then air-dried. The metallographic images were performed at high magnification (4X, 10X,40X,50X) with an optical microscope (AmScope model FMA050) equipped with a 5.1 MP digital camera 5 (see *Fig 3.3*).

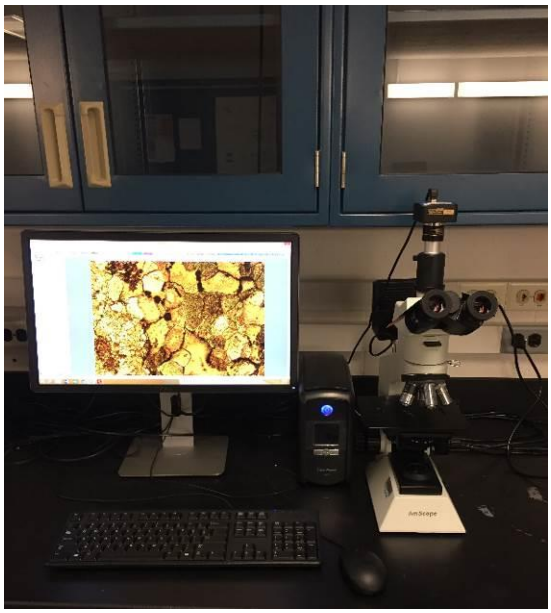

Figure 3.3 The optical microscope AmScope model FMA050.

3.4 Magnetization measurements

Magnetization measurements were done by using the Superconducting Quantum Interference Device (SQUID) magnetometer which is operated at a very low temperature (4.2 K) using liquid Helium. *Fig 3.4* shows the diagram of the (SQUID). In addition, the measurements were conducted in a temperature interval 5 to 400 K and the magnetic field up to 5 T. The SQUID has sensitivity between 0.000125 emu and 1.25 emu. So it is considered a very sensitive device to measure magnetization.

The procedures of the magnetization measurements are summarized in the following steps:

1- A small and known mass of the sample (<1 g) is placed in a plastic straw.
2- The plastic straw is tied to the end of transport rod which is made of Cu-Be.
3- Insert the rod in the sample space evacuated and filled with clean He gas.
4- After lowering the sample inside the liquid Helium Dewar, the sample is centered within the superconducting magnet.
5- The mechanical rod motion up and down causes a change in flux which is picked up by the SQUID coil and converted into magnetic moment.
6- The obtained data is recorded by automated MultiView software by Quantum Design, and the data is analyzed using Origin ™ software.

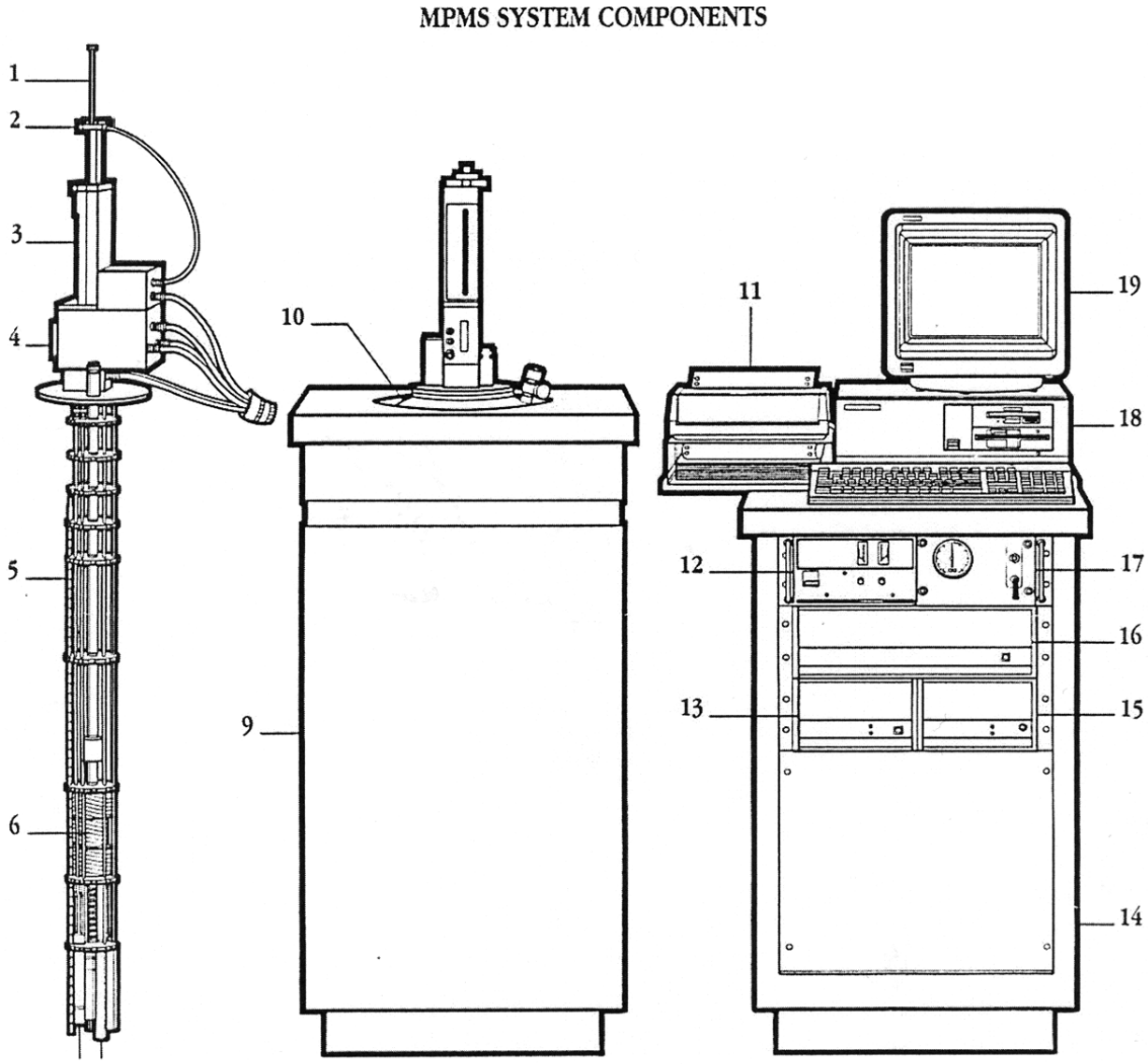

Figure 3.4 Diagram of the SQUID magnetometer by Quantum Design Inc. [61]

CHAPTER 4

Results and Discussions

In this chapter, we will discuss the experimental results in details for the two families of Heusler compounds Mn_2CoZ (Z= Ga, Ge, Sb) and Mn_2FeZ (Z= Si, Ge). For each family, we will identify the crystal structure by XRD, investigate their crystal grains with optical microscopy, and perform their magnetic measurements using SQUID.

4.1 Mn_2CoZ family

As mentioned in chapter three the three members of the Heusler family Mn_2CoZ are Mn_2CoGa, Mn_2CoGe, and Mn_2CoSb were prepared by arc-melting technique. In the following sections, we will discuss each sample individually.

4.1.1 Mn_2CoGa

A. The crystal structure of Mn_2CoGa

Fig 4.1 shows the room temperature powder X-ray diffraction pattern (XRD) of Mn_2CoGa powder annealed at 500 ^oC for two days. From the peaks positions we can infer that the sample matches the cubic lattice structure. The XRD patterns also explains that all principal reflection peaks of *bcc* structure are observed except secondary peaks such as (420). This result indicates that Mn_2CoGa forms pure (*bcc)* structure and the presence of (111) and (200) peaks which strongly suggests that the Mn_2CoGa alloy is formed in either L21 phase (Cu_2MnAl) or XA phase (Hg_2CuTi) structure. By using the experimental results and the equations (2.1) and (2.2), the lattice parameter of this alloy has been calculated to be (a= 5.869 Å) which is very close to prior experimental reports (a=5.873 Å) [1]. The XRD pattern of this sample is compared with the XA structure as shown *Fig 4.2(a)* and $L2_1$ structure as shown in *Fig 4.2(b)*

which are simulated by VESTA program and by using the experimental lattice parameter value (a= 5.869 Å). It is noted that the peaks positions in the Mn_2CoGa XRD patterns are matching positions for both types, while the relative intensities are different. It is well known that generally, the ordered/disordered structures can be identified by XRD analysis by using the ratio of the relative intensities between the super-lattice diffraction lines and the fundamental lines. The degree of $L2_1$ and B2 ordering can be identified by the ratio of the intensities of the (111) and (200) peaks to the intensity of the (220) peak respectively. It is noted that the relative intensities of the peaks for sample are close to match the intensities of the XA-type see Table 4.1 This leads us to identify the Mn_2CoGa alloy structure as the structure of inverse Heusler alloy which is agreement with the first principle calculation study [54,62].

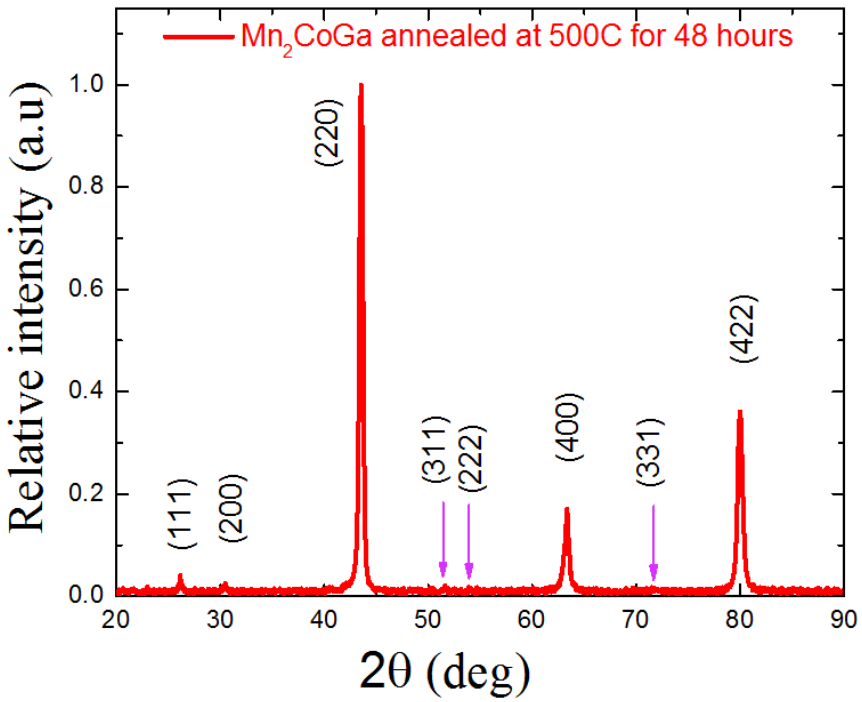

Figure 4.1 Room temperature X-ray diffraction patterns of Co_2MnGa alloy annealed at 500°C for 2 days.

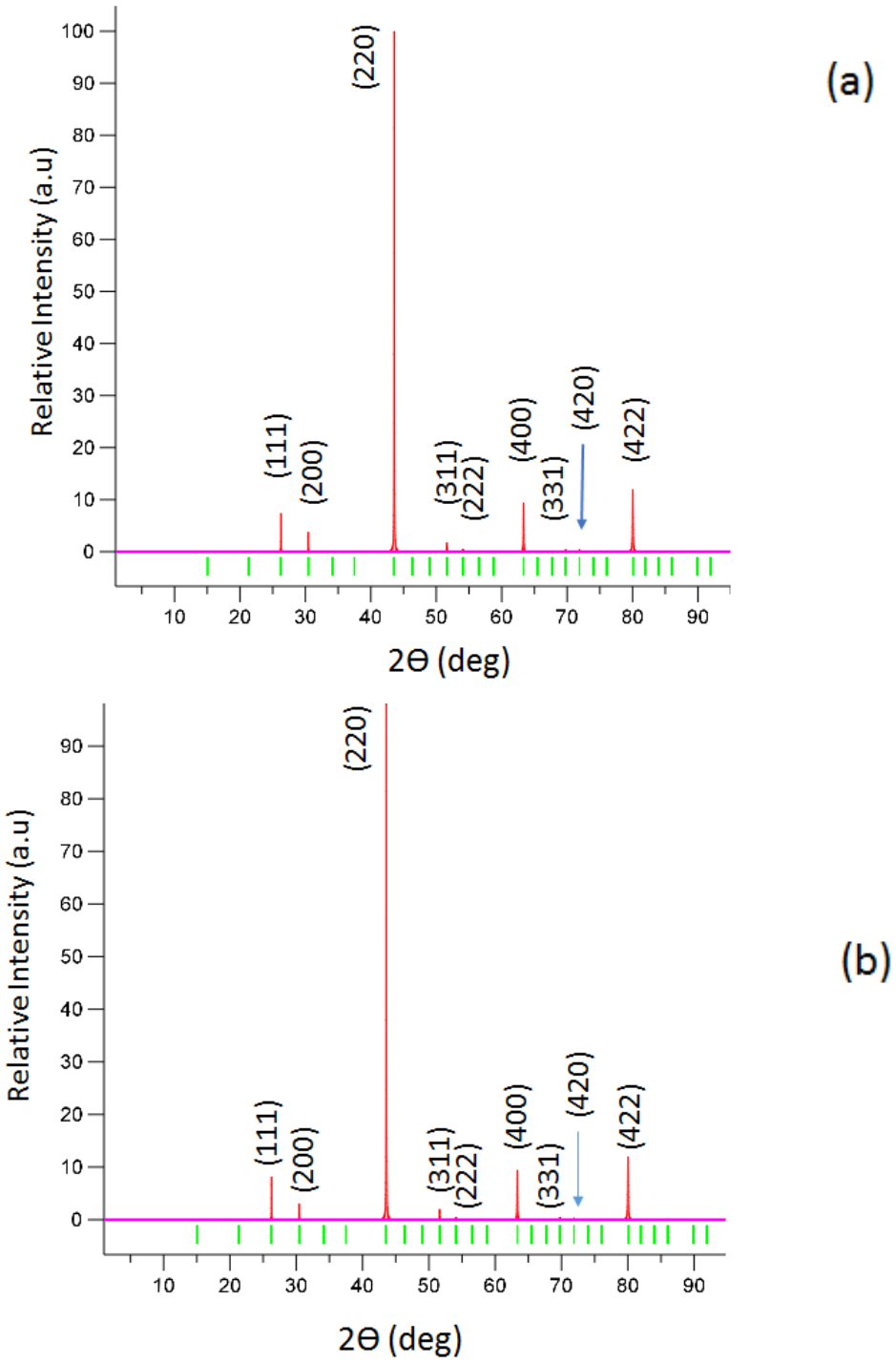

Figure 4.2 Simulated X-ray diffraction patterns by VESTA program for (a=5.869 A) of (a) Hg_2CuTi-type structure which is represented inverse Heusler alloy with space group 216, $F\bar{4}3m$. (b) Cu_2MnAl-type structure which is represented $L2_1$ structure with space group 225, $Fm\bar{3}m$.

Table 4.1 XRD relative intensity peaks of (Mn_2CoGa annealed at 500 ^oC for 48 hours, XA- type and $L2_1$-type simulated by VESTA program and using the lattice parameter (a= 5.869 Å).

2θ (deg)	(hkl)	Relative Intensity (a.u) for Mn_2CoGa annealed at 500C for 2days	Relative Intensity (a.u) for XA-type	Relative Intensity (a.u) for $L2_1$-type
26.16	(111)	4.08	7.70	8.60
30.48	(200)	2.13	5.87	4.68
43.56	(220)	100	100	100
51.68	(311)	0.71	0.96	1.08
53.92	(222)	0.08	0.90	0.71
63.36	(400)	15.28	26.48	26.48
80	(422)	34.29	11.29	11.29

In addition*, Fig 4.3* and *Fig 4.4* show that the powder X-ray diffraction patterns of Mn_2CoGa annealed for 48 hours at different temperatures (500 ^oC, 700 ^oC, and 900 ^oC). We can note that the $L2_1$ super-lattice peak is clearly observed only at 500 ^oC and 700^oC and the relative intensity at 500 ^oC is higher than that at 700 ^oC. Also, the B2 super-lattice peak is clear observed only at 500 ^oC and 900 ^oC with high relative intensity at 500 ^oC. This observation leads us to confirm that the crystal structure of the Mn_2CoGa is formed the XA structure with high order when annealed the sample at 500^oC for 2 days.

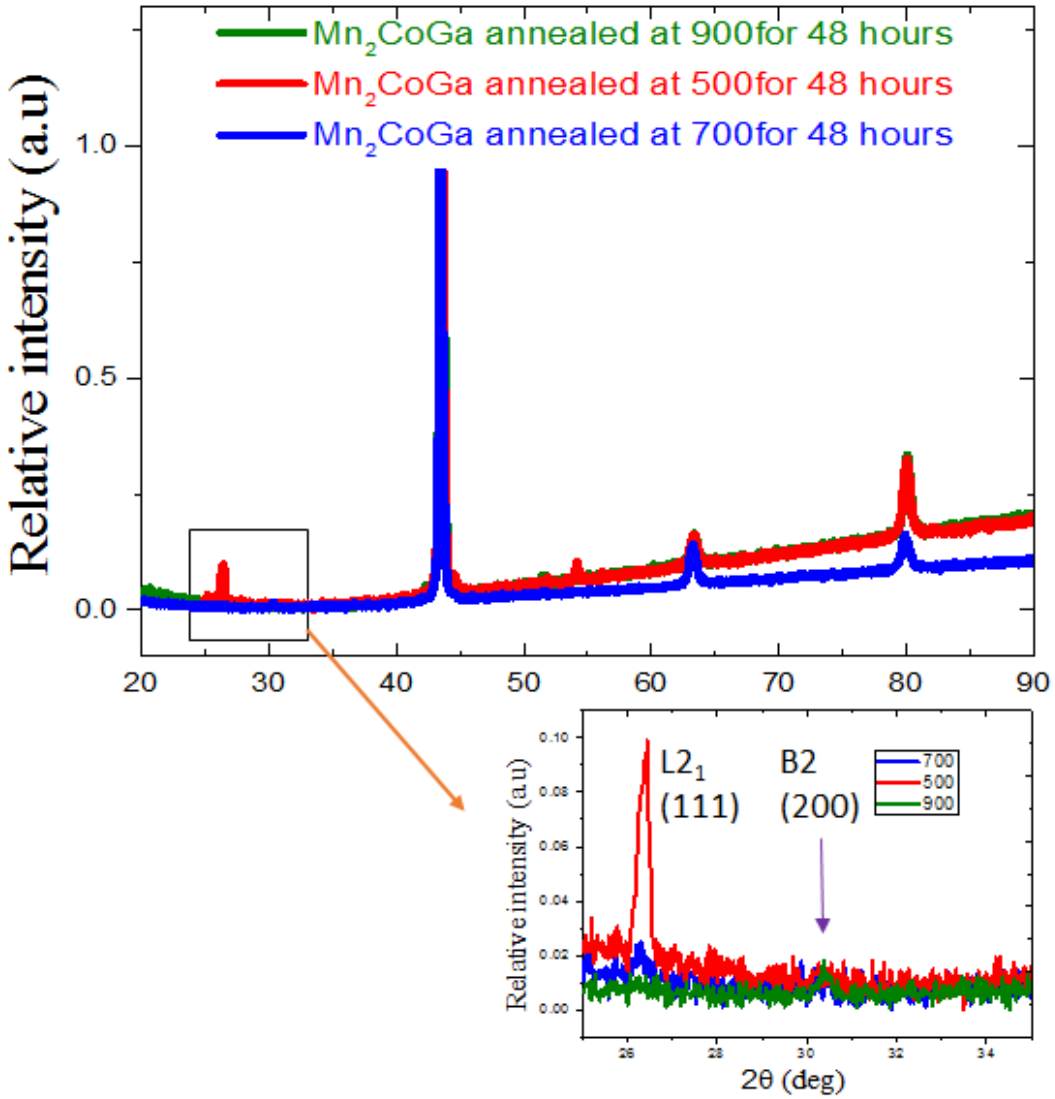

Figure 4.3 The powder X-ray diffraction patterns of Mn_2CoGa annealed for 48 hours at different temperatures (500 ^oC, 700 ^oC, and 900 ^oC) illustrating the super-lattices peaks (L21, B2, and A2).

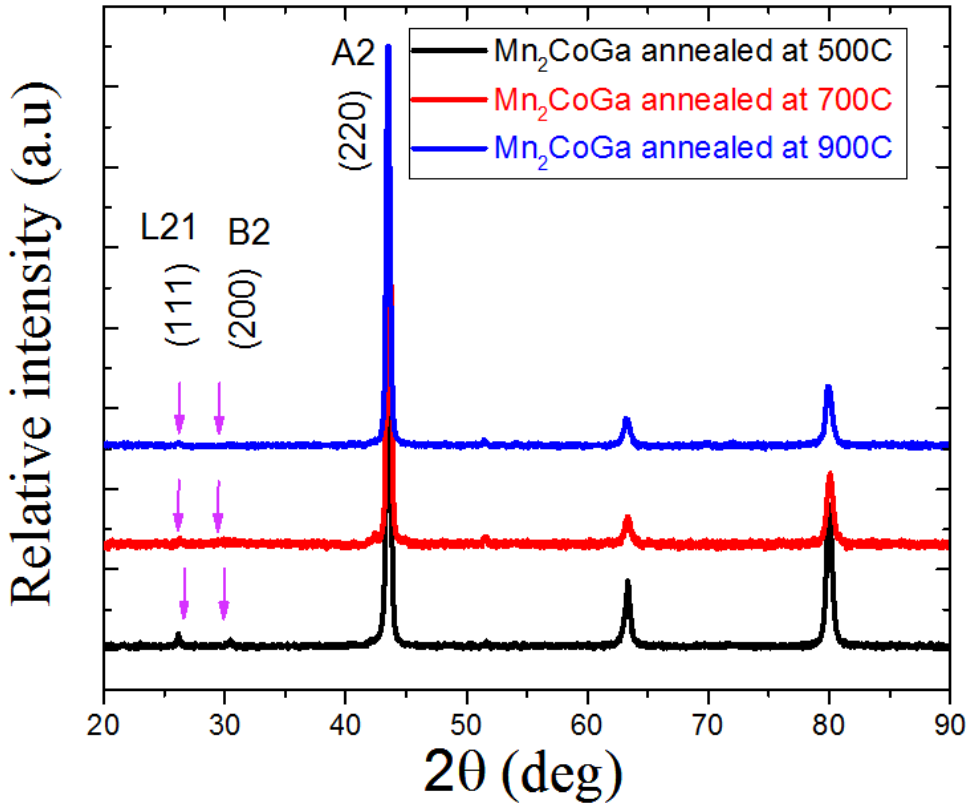

Figure 4.4 The relative intensity of $L2_1$ and B2 peaks in the powder X-ray diffraction patterns of Mn_2CoGa annealed for 2 days at different temperatures (500 ^oC, 700 ^oC, and 900 ^oC).

B. The magnetic properties of the Mn_2CoGa

The preceding discussion is concerned with the crystal structure of the Mn_2CoGa, we now turn to the magnetic properties. The temperature dependence of the magnetization M(T) of Mn_2CoGa on heating and cooling cycles at the range of 5^oK to 400 ^oK in the presence of magnetic field of 100 Oe is shown in *Fig 4.5*. The field

dependence of magnetization M(H) of Mn_2CoGa measured at T =5^o K with change in field up to 5T is shown in Figure 4.6.

It is clear that the magnetization is easy to saturate and it is saturated in the magnetic field of about (2000 Oe). The saturation value is obtained to be (47 *emu/g*) and converted to (2.007 μ_B /*fu*) this value is very close to the integer value 2. This result is consistent with Slater-Pauling rule, where the total magnetic moment of Mn_2CoGa is measured depending on the equation $m_t = N_V - 24$ where m_t is the total magnetic moment and N_V is the total number of valence electron since the Mn_2CoGa has N_V =26 then the m_t =2 μ_B /*fu* [49]. This value (m_t) was predicted in a theoretical study [62] that suggested that a compound is considered an ideal half-metal ferrimagnet when the lattice constant of the Mn_2CoZ family is within the range of 5.4 and 5.9 Å, which is consistent with our results.

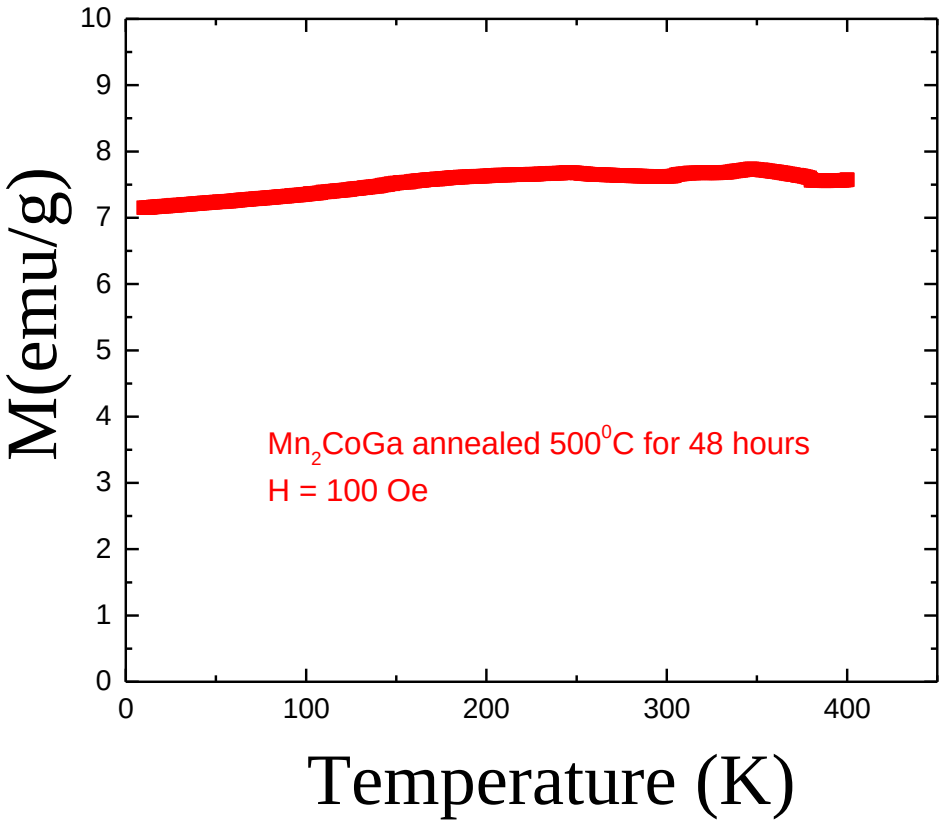

Figure 4.5 The temperature dependence of the magnetization M(T) of Mn_2CoGa annealed for 2 days at 500 ^oC on heating and cooling under the magnetic field of 100 Oe.

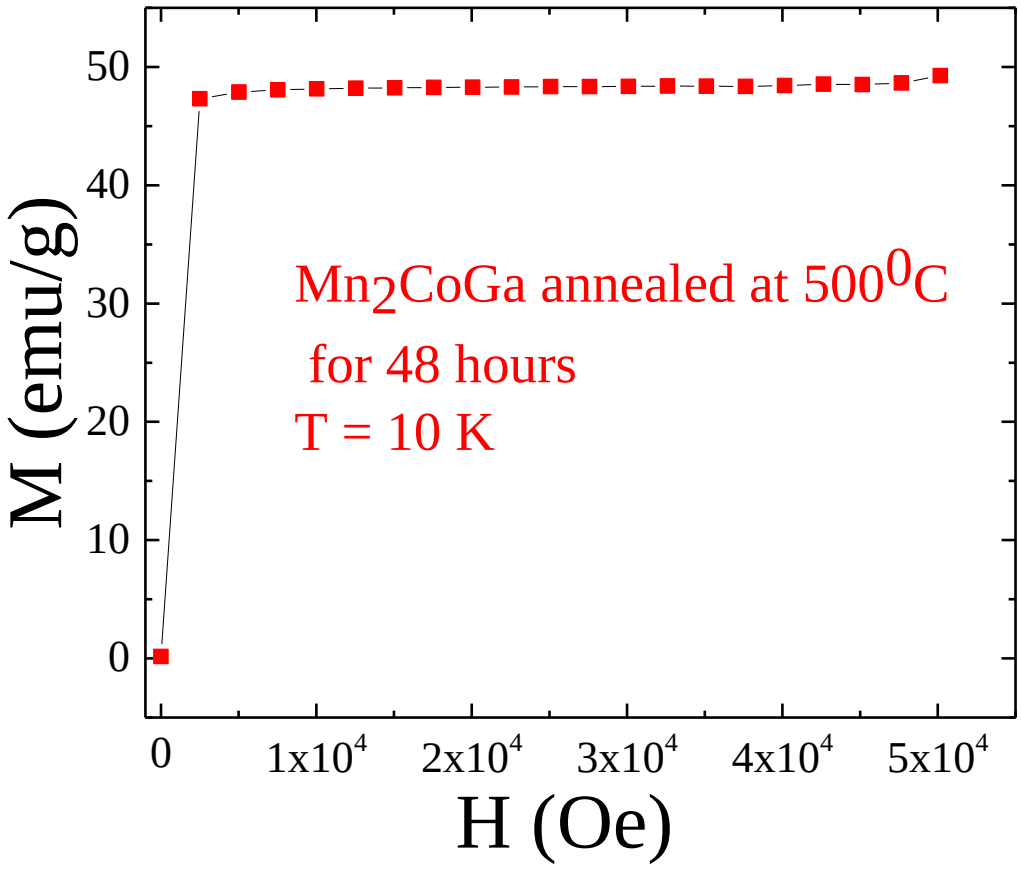

Figure 4.6 M(H) curves of Mn_2CoGa annealed for 2 days at 500 ^oC measured at T = 5 K with change in magnetic field up to 5T.

C. The microstructure of Mn2CoGa

The microstructure observation was conducted by the optical microscope, *Fig 4.7* shows that the optical images of Mn_2CoGa annealed at 500 ^oC for 2 days. This image is already showing a single-grain microstructure which means that the synthesize of this alloy is successfully accomplished and this image is fully homogenized alloy which is also most probably single phase.

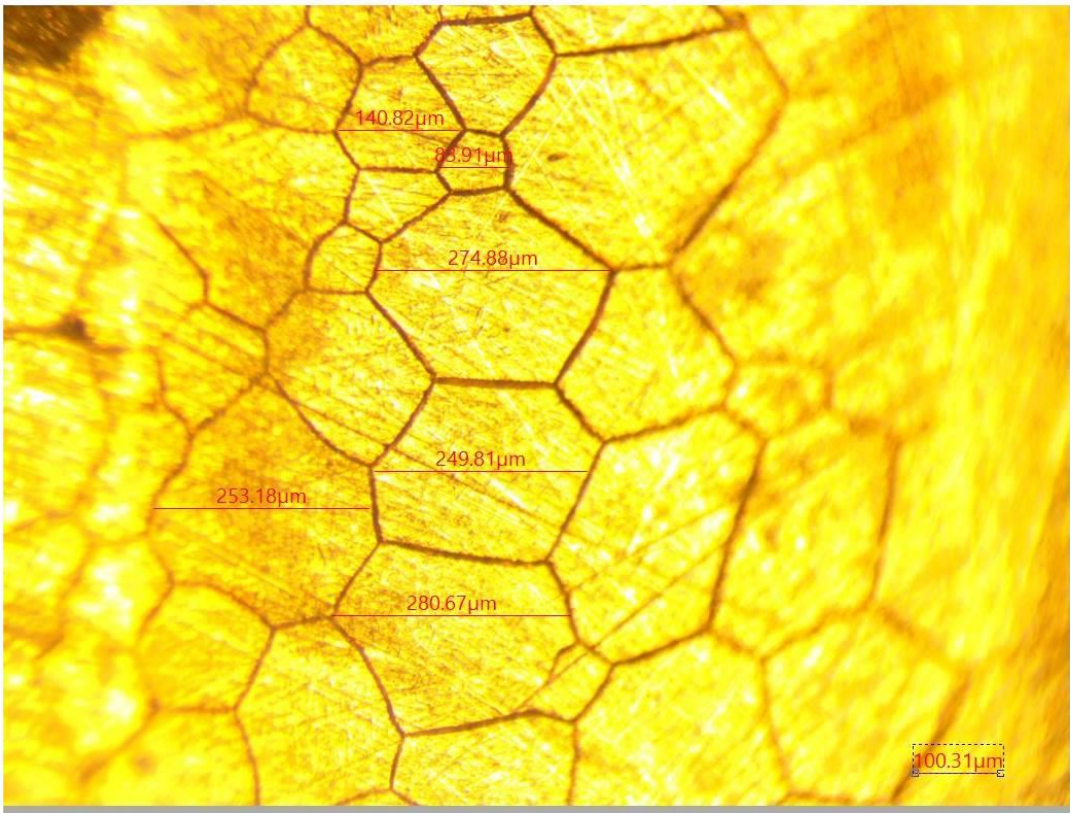

Figure 4.7 The optical image of the Mn_2CoGa annealed at 500 ^oC for 2 days after etching the sample by using Marble's reagent for 30 seconds.

4.1.2 Mn_2CoGe and Mn_2CoSb

By the same preparation technique of Mn_2CoGa using the arc-melting, the Mn_2CoGe and Mn_2CoSb are prepared. The XRD measurements for both samples are carried out at room temperature for the samples which annealed at 500, 700, and 900^oC for 2 days. *Fig 4.8(a)* explains the XRD pattern of Mn_2CoSb alloy annealed at 500^oC for 2 days. It is clearly shown that many peaks are observed in the XRD pattern apart from the principal cubic structure diffraction peaks. These peaks imply that there are other phases are formed. It indicates that homogenization has not been achieved using our heat treatment. We can attribute it to the heavier atomic weight of antimony which leads to low diffusion rate and low driving force for homogenization. Our XRD pattern agrees with previous experimental study [51] where a subsequent melt-spinning treatment was found necessary in producing a pure cubic phase as shown in Fig 4.8(b). Similar multiphase results were obtained for Mn_2CoGe see *Fig 4.9*. Therefore, we conclude that arc-melting technique is not suitable to prepare all Mn_2-based Heusler alloys.

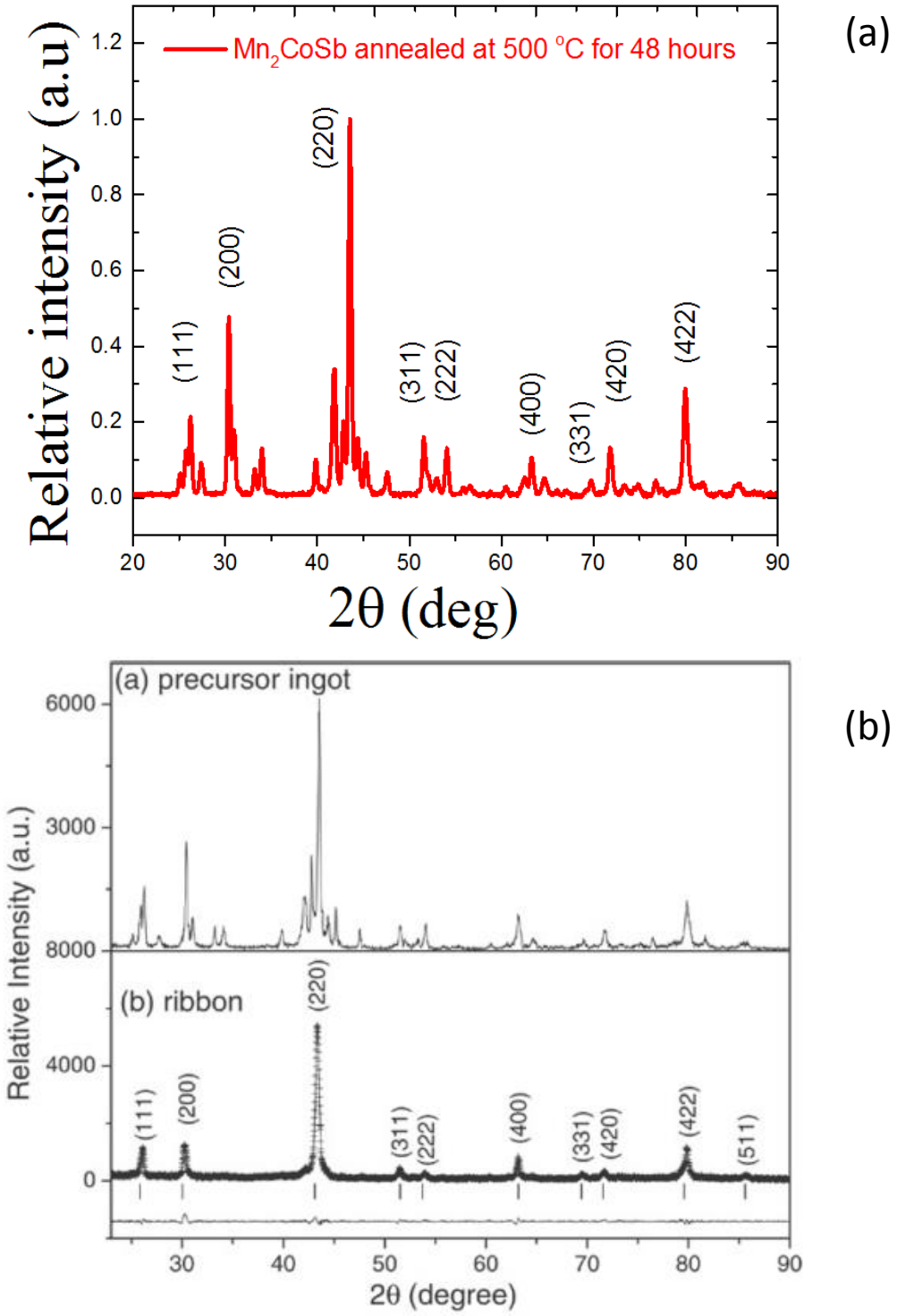

Figure 4.8 (a) Our X-ray diffraction patterns of Mn_2CoSb alloy annealed at 500°C for 2 days. (b) X-ray diffraction patterns of Mn_2CoSb precursor ingot by using the arc-melting and the melt-spun samples in different experimental study [51].

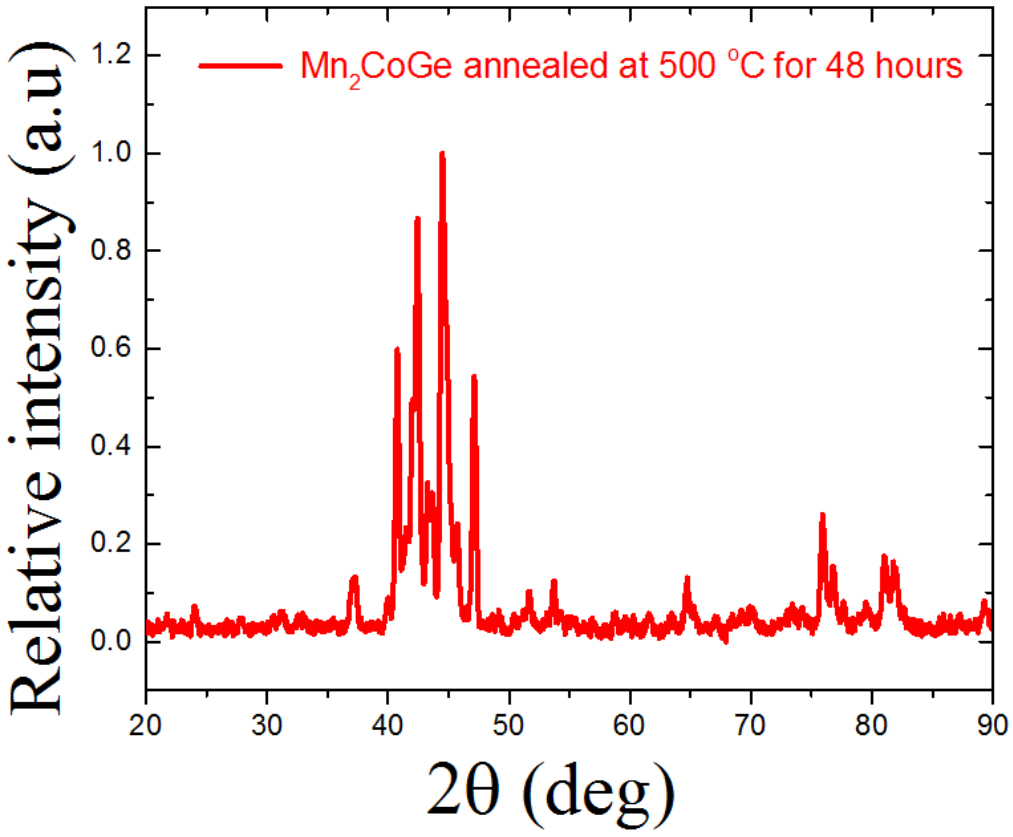

Figure 4.9 Room temperature X-ray diffraction patterns of Mn_2CoGe alloy annealed at 500°C for 2 days.

4.2 Mn_2FeZ family

Theoretical studies indicate that within the Mn_2FeZ family, Mn_2FeSi and Mn_2FeGe are stable [35]. There are no reports of growing these alloys. In this section, we will discuss the data results of the experimental study of this family individually.

4.2.1 Mn_2FeSi

A. The crystal structure of Mn_2FeSi

Fig 4.10 shows the room temperature XRD patterns of arc-melt Mn_2FeSi samples annealed for 2 days at different temperatures (500 ^oC, 600 ^oC, and 800^oC). The principal peaks of the cubic structure are observed and it can be indexed with this structure. Some nonsystematic peaks are observed at $2\theta = 43^o$, 46^o and 48^o. This indicates that other phases are also formed, and a reasonable match for oxides of manganese and iron. At higher annealing temperatures, the cubic heusler peaks are stronger. The oxide phases also become strong at higher temperatures. Therefore, a low temperature (500^{0}C) was chosen for most experimental investigations and analysis. By using this data of the XRD pattern, the lattice parameter was calculated and found to be a= 5.682 Å (see Table 4.2).

We observe many new peaks at higher temperatures that implies 500 ^{o}C is the best temperature to synthesize this alloy and we need to find out the best annealing time. Thus, the sample was annealed at 500^{0}C for different times 2, 5, and 10 days.

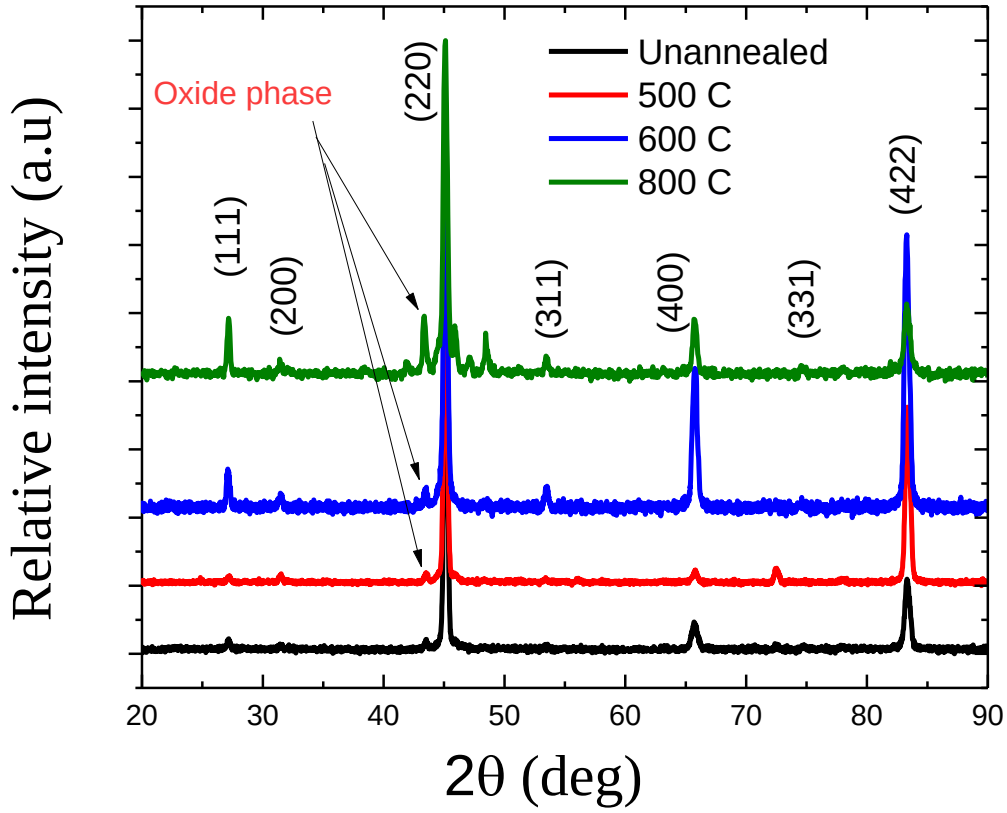

Figure 4.10 The powder X-ray diffraction patterns of Mn_2FeSi annealed for 2 days at different temperatures (500 ^oC, 600 ^oC, and 800 ^oC).

Table 4.2 The relative intensities and the lattice parameter of Mn_2FeSi annealed at 500°C for 2 days.

2θ (deg)	(hkl)	Rel. I. (a.u) for annealed for 2 days	Lattice parameter a (Å)
27.2	(111)	1.72	5.693
31.56	(200)	2.33	5.675
45.12	(220)	100	5.681
53.48	(311)	0.74	5.677
65.70	(400)	3.12	5.682
72.56	(331)	3.78	5.682
83.3	(422)	52.6	5.684
The average lattice parameter (a=5.682 Å)			

The XRD pattern of Mn_2FeSi annealed at 500^0C for different times 2, 5, and 10 days is shown in *Fig 4.11 (a)*. It is easy to note that the sample which annealed for 10 days has high relative intensity for the $L2_1$ (111) peak, while the B2 (200) peaks almost have the same relative intensity value as shown in *F*ig. 4.11 (b) and Table 4.3.

Table 4.3 XRD relative intensity peaks of (Mn_2FeSi annealed at 500 ^oC for 2,5,10 days, the XA- type and the $L2_1$-type simulated by VESTA program and using the lattice parameter (a= 5.682 Å).

2θ (deg)	(hkl)	R.I. (a.u) annealed for 2 days	R.I. (a.u) annealed for 5 days	R.I. (a.u) annealed for 10 days	R.I. (a.u) for XA-type	R.I. (a.u) for $L2_1$-type
27.2	(111)	1.72	4.86	6.32	7.93	8.86
31.56	(200)	2.33	1.17	2.15	6.01	4.78
45.12	(220)	100	100	100	100	100
53.48	(311)	0.74	3.81	2.72	0.94	1.06
65.70	(400)	3.12	9.03	6.26	25.9	25.9
72.56	(331)	3.78	1.11	0.8	0.27	0.30
83.24	(422)	52.6	27.97	39.48	11.11	11.11

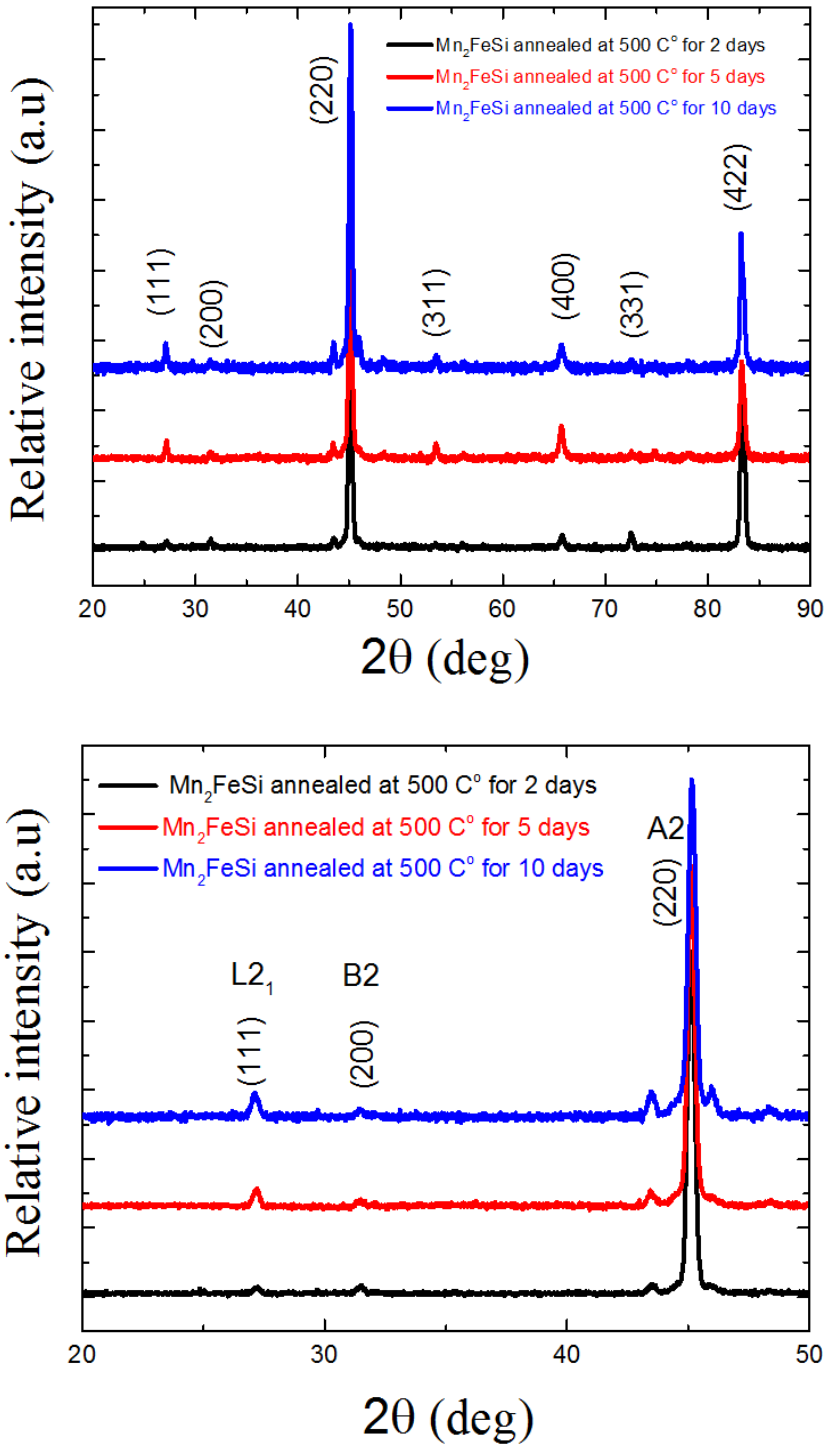

Figure 4.11 (a) The XRD pattern of Mn_2FeSi annealed at 500^0C for different times 2, 5, and 10 days. (b) The XRD super-lattice peaks $L2_1$, B2, and A2.

To study the degree of ordering in the sample, *Fig 4.12* shows the degree of ordering $L2_1$ and B2 for Mn_2FeSi annealed at 500 ^oC for different times: 2,5, and 10 days. We can note that the ratio of the (111) peak intensity to the intensity of the (220) peak improves with increasing the annealing time and for the sample annealed for 10 days is close to the theoretical limit of the relative intensity for the simulated XA at a=5.682 Å. This result implies that the best condition to synthesize the Mn_2FeSi alloy with high atomic order is annealing the sample at 500^oC for 10 days.

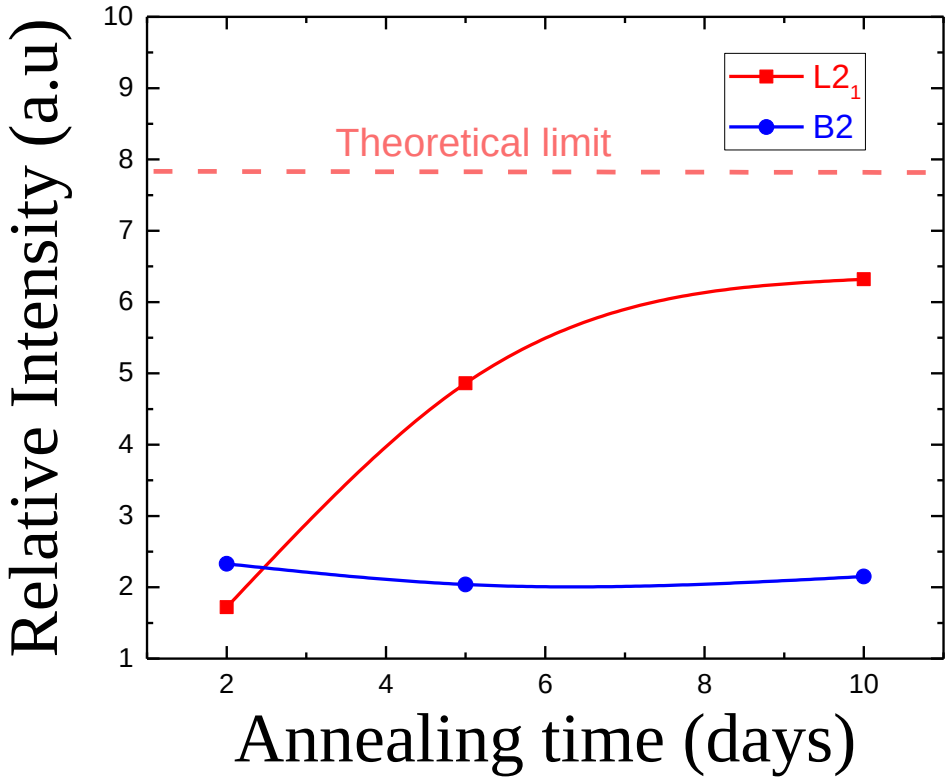

Figure 4.12 Degree of ordering $L2_1$ and B2 for Mn_2FeSi annealed at 500 ^oC for different times: 2,5, and 10 days.

B. The microstructure of Mn_2FeSi

Fig 4.13 shows that the optical images of Mn_2FeSi annealed at 500 ^oC for 2 days. These images show crystal grains that indicate a good microstructure. We can conclude that our synthesis of this alloy is successful at 500 ^oC for 2 days.

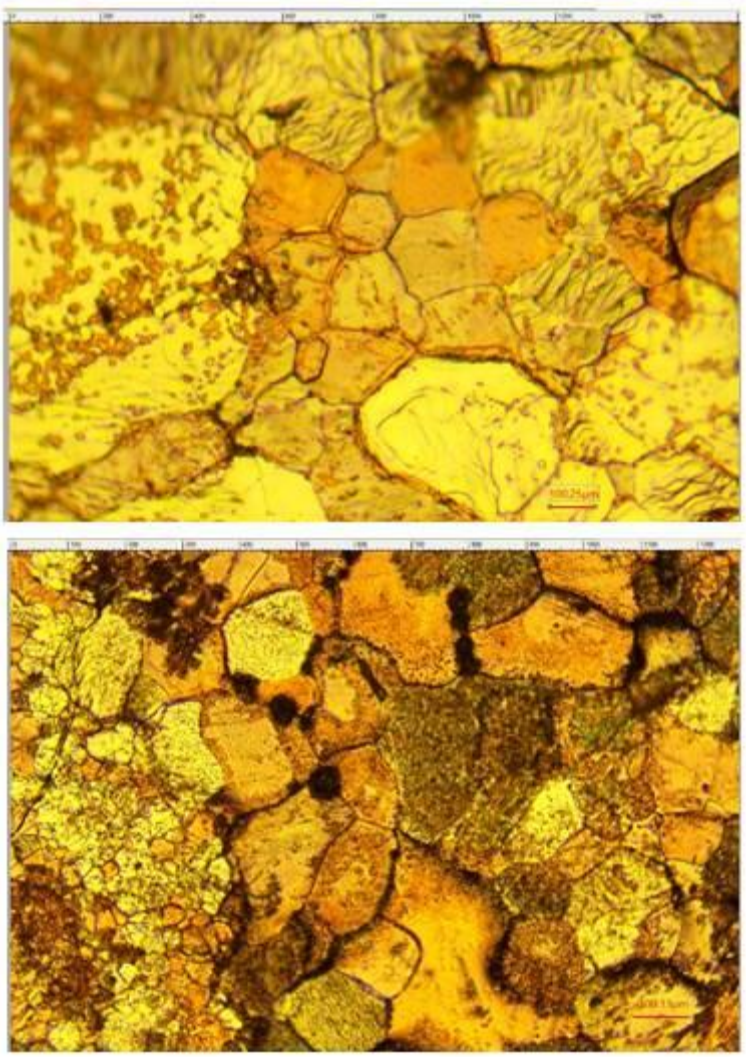

Figure 4.13 Two of the optical images of the Mn_2FeSi annealed at 500 ^oC for 2 days after etching the sample by using Marble's reagent for 30 seconds.

4.2.2 Mn_2FeGe

Similarly, we prepared the Mn_2FeGe sample using arc-melting and by using the X-ray diffraction method to study it crystal structure. We annealed the Mn_2FeGe at different temperatures (500 and 900ºC) for two days as shown in *Fig 4.14*. Contrary to Mn2FeSi, The XRD- pattern of Mn_2FeGe show more multi-phases at 500ºC than 900ºC. It implies that this sample needs to be annealed at high temperature for long time.

In addition, the optical images of the sample annealed at 900 ºC for 2 days are shown in *Fig 4.15* which indicates that there are some grains but the sample is still

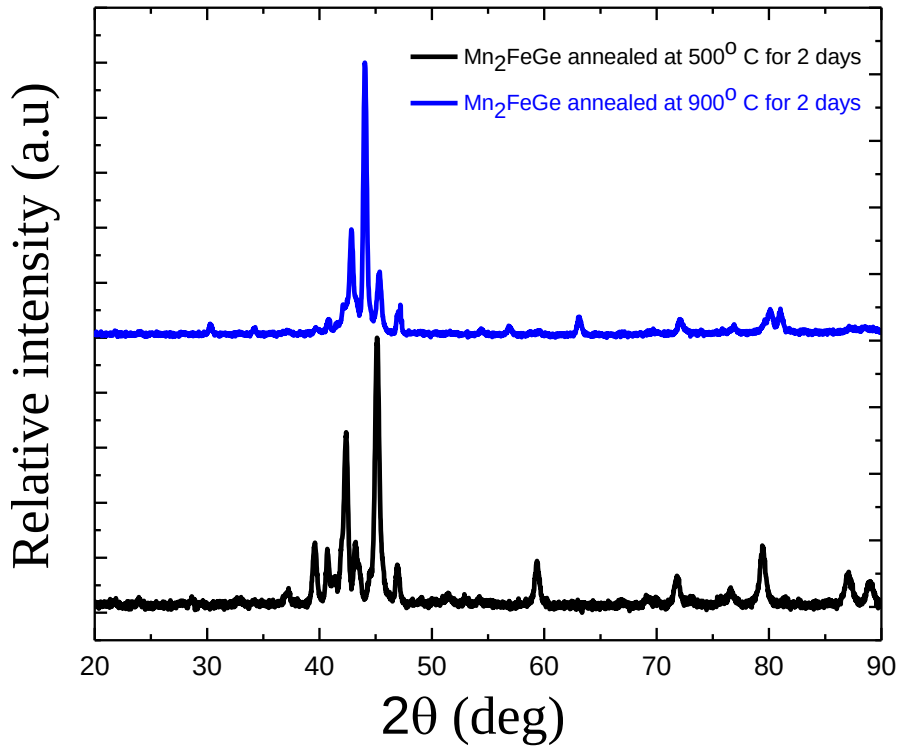

Figure 4.14 The powder X-ray diffraction patterns of Mn_2FeGe annealed for 2 days at different temperatures (500 ºC and 900 ºC).

inhomogeneous. In short, we need to heat it more to move and develop grains instead of dendrites.

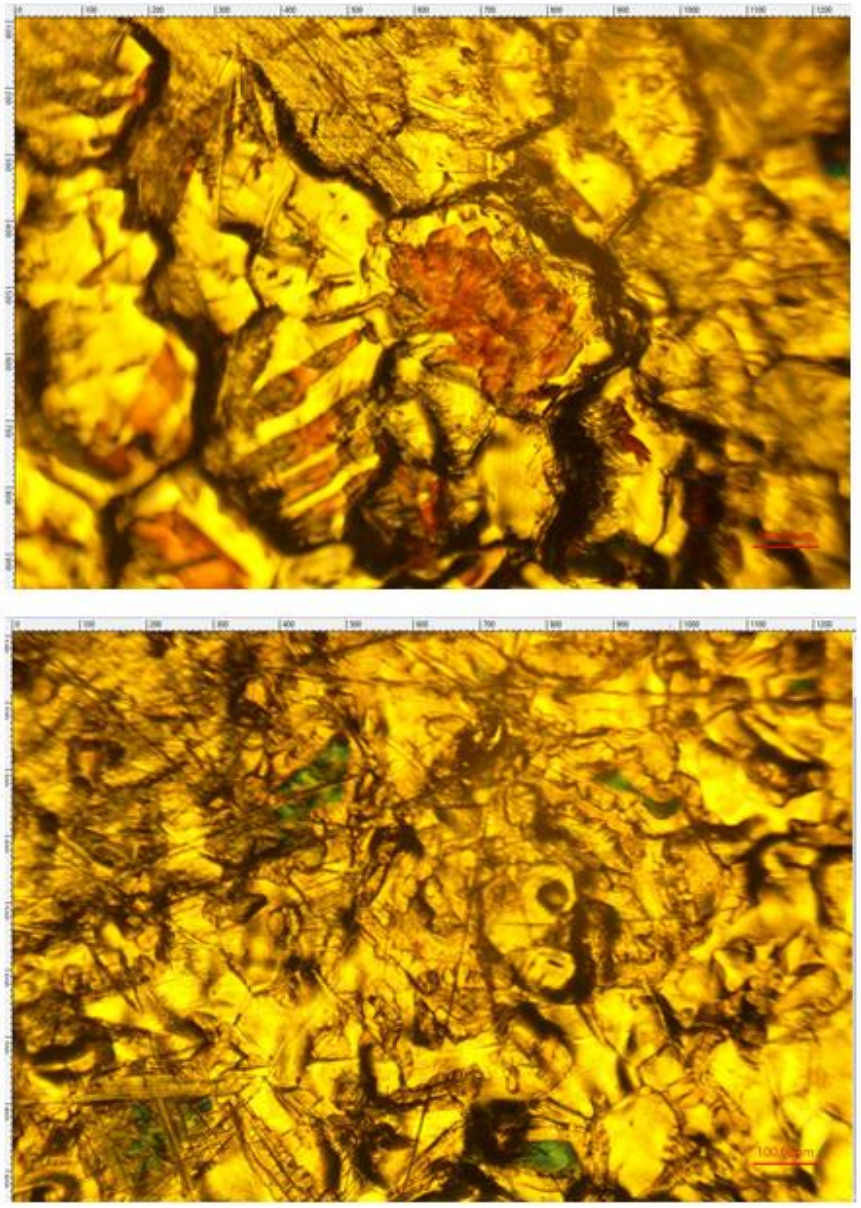

Figure 4.15 Optical images of the Mn_2FeGe annealed at 900 ^oC for 2 days after etching the sample by using Marble's reagent for 30 seconds.

CHAPTER 5

CONCLUSION

In conclusion, two different families of Mn-based Heusler compounds have been studied: Mn_2CoZ (Z= Ga, Sb, Ge) and Mn2FeZ(Z=Si,Ge), with the latter being new materials. The samples were prepared by using the arc-melting technique and the growth conditions and the metallography of these families were investigated. The crystal structure of the samples was studied by the X-ray diffraction method. The summary of the experimental studies for all samples is shown in Table 5.1.

Table 5.1 Illustration of the summary of the experimental measurements done in this study.

Sample fabricated	Cubic phase stabilized	Lattice parameter a (Å)	Experimental magnetic measurements	Comments
Mn_2CoGa	Yes	5.869	2.007 μ_B /*fu*	Possible with arc melting
Mn_2CoGe	No	Estimated (a) 5.754	-	Requires further annealing treatment
Mn_2CoSb	No	Estimated (a) 5.874	-	Does not working with arc-melting
Mn_2FeSi	Yes	5.682	Antiferromagnetic behavior	Possible with arc melting
Mn_2FeGe	No	Estimated (a) 5.814	-	Required further annealing treatment

The XRD pattern of Mn_2CoGa showed that a cubic crystal structure is formed. The super-lattice diffraction peaks (111) and (200) are observed only in the XRD patterns in the samples annealed at 500ºC for 48 hours and the lattice parameter of this alloy was calculated to be a= 5.869 Å. The relative intensities of the peaks for sample are close to the calculated intensities of XA phase by using VESTA program which strongly suggests that the Mn_2CoGa alloy is formed as a highly ordered Inverse Heusler structure of the space group $F\bar{4}3m$, number (216) and it is stable after annealing the sample at 500ºC for 48 hours.

The magnetic properties and the microstructure observations of the Mn_2CoGa alloys have been studied. The results showed that the saturation value is obtained to be (47 *emu/g*) and converted to (2.007 μ_B /*fu*) which is matching the Slater-Pauling rule value $m_t = N_V - 24$ where N_V of Mn_2CoGa is 26. Also, the microstructure analysis of Mn_2CoGa alloys showed a single-grain microstructure which means that the synthesize of this alloy is successful.

Mn_2CoSb and Mn_2CoGe have been investigated and the XRD pattern of arc-melt samples of these alloys annealed at 500ºC for 2 days. From our results, we conclude that arc-melting technique may not be suitable to prepare these alloys.

The new family of the Mn-based alloys (Mn_2FeSi and Mn_2FeGe) have been studied. Theoretical results show that Mn_2FeSi alloys are promising half-metal Heusler alloys. Synthesis of Mn_2FeSi was investigated under various conditions of the annealing temperature and time. It was found that the sample annealed at 500ºC for 48 hours provided a cubic Heusler phase with only weak oxidized secondary phases. The measured lattice parameter was 5.682 Å. In addition, the ratio of the (111) peak intensity

to the intensity of the (220) peak improved with increasing the annealing time and was very close to the calculated relative intensity of the inverse Heusler (XA) phase. Therefore, we conclude that the sample annealed at 500^{o}C for 10 days produced a higher degree of atomic ordering. Optical images of the Mn_2FeSi alloy showed some crystal grains.

Finally, the XRD patterns of Mn_2FeGe alloy explained that with an increase in annealing temperature, an elimination of some phases and an improvement of the cubic Heusler structure are noted. For future work, it is recommended to anneal samples for longer time at higher temperature.

REFERENCES

[1] R. Y. Umetsu and T. Kanomata, Physics Procedia **75**, 890 (2015).

[2] T. Graf, C. Felser, and S. S. P. Parkin, Progress in Solid State Chemistry **39**, 1 (2011).

[3] A. D. Kent and D. C. Worledge, Nat Nanotechnol **10**, 187 (2015).

[4] S. Parkin and S. H. Yang, Nat Nanotechnol **10**, 195 (2015).

[5] H. S. Wong and S. Salahuddin, Nat Nanotechnol **10**, 191 (2015).

[6] S. Wolf, D. Awschalom, R. Buhrman, J. Daughton, S. Von Molnar, M. Roukes, A. Y. Chtchelkanova, and D. Treger, Science **294**, 1488 (2001).

[7] G. E. Moore, Electronics **38** (1965).

[8] O. Gutfleisch, M. A. Willard, E. Bruck, C. H. Chen, S. G. Sankar, and J. P. Liu, Adv Mater **23**, 821 (2011).

[9] P. Varshney and H. Agrawal, (2014).

[10] H. Ohno, in *Device Research Conference, 2006 64th* (IEEE, 2006), pp. 9.

[11] M. E. Flatte, IEEE Transactions on Electron Devices **54**, 907 (2007).

[12] M. N. Baibich, J. M. Broto, A. Fert, F. Nguyen Van Dau, F. Petroff, P. Etienne, G. Creuzet, A. Friederich, and J. Chazelas, Phys Rev Lett **61**, 2472 (1988).

[13] J. S. Moodera, L. R. Kinder, T. M. Wong, and R. Meservey, Phys Rev Lett **74**, 3273 (1995).

[14] T. Miyazaki and N. Tezuka, Journal of Magnetism and Magnetic Materials **139**, L231 (1995).

[15] S. Ikeda, J. Hayakawa, Y. M. Lee, R. Sasaki, T. Meguro, F. Matsukura, and H. Ohno, Japanese journal of applied physics **44**, L1442 (2005).

[16] W. Shen, D. Mazumdar, X. Zou, X. Liu, B. D. Schrag, and G. Xiao, Applied Physics Letters **88**, 182508 (2006).

[17] M. Julliere, Physics letters A **54**, 225 (1975).

[18] J. S. Moodera and G. Mathon, Journal of magnetism and magnetic materials **200**, 248 (1999).

[19] E. Y. Tsymbal, O. N. Mryasov, and P. R. LeClair, Journal of Physics: Condensed Matter **15**, R109 (2003).

[20] M. F. M. de Groot R. A., VAn Engen P.G. and Buschow K. H. J., physical Review letters **50**, 2024 (1983).

[21] C. M. Fang, G. De Wijs, and R. De Groot, Journal of Applied Physics **91**, 8340 (2002).

[22] J. F. Igor Z˘utic´, and S. Das Sarma, Reviews of Modern Physics **76**, 323 (2004).

[23] J. Barth *et al.*, Philos Trans A Math Phys Eng Sci **369**, 3588 (2011).

[24] T. O. Y. Tomioka, Y. Okimoto, R. Kumai, K.-I. Kobayashi, and Y. Tokura, Physical Review B **61**, 422 (2000).

[25] K. Schwarz, Journal of Physics F: Metal Physics **16**, L211 (1986).

[26] J. B. Goodenough, Progress in Solid State Chemistry **5**, 145 (1971).

[27] H. F. D. Orgassa, T. C. Schulthess and W. H. Butler, Physical Review B **60**, 13237 (1999).

[28] J. Coey and C. Chien, Mrs Bulletin **28**, 720 (2003).

[29] R. Yamamoto, Y. Moritomo, and A. Nakamura, Physical Review B **61**, R5062 (2000).

[30] K. A. Kilian and R. H. Victora, Journal of Applied Physics **87**, 7064 (2000).

[31] S. Datta and B. Das, Applied Physics Letters **56**, 665 (1990).

[32] G. Binasch, P. Grünberg, F. Saurenbach, and W. Zinn, Physical Review B **39**, 4828 (1989).

[33] Y. Miura, K. Nagao, and M. Shirai, Physical Review B **69** (2004).

[34] T. M. Nakatani, A. Rajanikanth, Z. Gercsi, Y. K. Takahashi, K. Inomata, and K. Hono, Journal of Applied Physics **102**, 033916 (2007).

[35] J. Ma, Jiangang He, Munira, Kamaram, Xie, Yunkun,, S. Keshavarz, C. Wolverton, A. W. Ghosh, and W. Butler, William H. Butler, (2016).

[36] S. W. Heusler F., Haupt E. Verh DPG **5**, 220 (1903).

[37] V. Heusler F., DPG **5**, 219 (1903).

[38] S. Chadov, X. Qi, J. Kübler, G. H. Fecher, C. Felser, and S. C. Zhang, Nature materials **9**, 541 (2010).

[39] Y. Nishino, M. Kato, S. Asano, K. Soda, M. Hayasaki, and U. Mizutani, Physical review letters **79**, 1909 (1997).

[40] P. Webster, Landolt-Börnstein New Series **3**, 75 (1988).

[41] H. Luo, L. Yang, B. Liu, F. Meng, and E. Liu, Physica B: Condensed Matter **476**, 110 (2015).

[42] C. Kittel and D. F. Holcomb, American Journal of Physics **35**, 547 (1967).

[43] S. Picozzi, A. Continenza, and A. J. Freeman, Physical Review B **69**, 094423 (2004).

[44] M. P. Raphael *et al.*, Physical Review B **66** (2002).

[45] Y. Takamura, R. Nakane, and S. Sugahara, Journal of Applied Physics **107**, 09B111 (2010).

[46] B. D. Cullity and C. D. Graham, *Introduction to magnetic materials* (John Wiley & Sons, 2011).

[47] J. C. Slater, Physical Review **49**, 537 (1936).

[48] L. Pauling, Physical Review **54**, 899 (1938).

[49] L. Wollmann, S. Chadov, J. Kübler, and C. Felser, Physical Review B **90**, 214420 (2014).

[50] R. Weht and W. E. Pickett, Physical Review B **60**, 13006 (1999).

[51] X. Dai, G. Liu, L. Chen, J. Chen, and G. Wu, Solid State Communications **140**, 533 (2006).

[52] H. Luo, Z. Zhu, G. Liu, S. Xu, G. Wu, H. Liu, J. Qu, and Y. Li, Journal of Magnetism and Magnetic Materials **320**, 421 (2008).

[53] S. Wurmehl, H. C. Kandpal, G. H. Fecher, and C. Felser, Journal of Physics: Condensed Matter **18**, 6171 (2006).

[54] G. D. Liu, X. F. Dai, H. Y. Liu, J. L. Chen, Y. X. Li, G. Xiao, and G. H. Wu, Physical Review B **77** (2008).

[55] Y. Xin, H. Hao, Y. Ma, H. Luo, F. Meng, H. Liu, E. Liu, and G. Wu, Intermetallics **80**, 10 (2017).

[56] M. Meinert, J. M. Schmalhorst, and G. Reiss, J Phys Condens Matter **23**, 116005 (2011).

[57] V. Alijani, J. Winterlik, G. H. Fecher, and C. Felser, Applied Physics Letters **99**, 222510 (2011).

[58] K. Minakuchi, R. Y. Umetsu, K. Kobayashi, M. Nagasako, and R. Kainuma, Journal of Alloys and Compounds **645**, 577 (2015).

[59] R. Umetsu, K. Saito, K. Ono, T. Ishigaki, T. Minakuchi, M. Nagasako, and R. Kainuma, in *2015 IEEE Magnetics Conference (INTERMAG)* (IEEE, 2015), pp. 1.

[60] H. Z. Luo, H. W. Zhang, Z. Y. Zhu, L. Ma, S. F. Xu, G. H. Wu, X. X. Zhu, C. B. Jiang, and H. B. Xu, Journal of Applied Physics **103**, 083908 (2008).

[61] User's Manual, Quantum Design, Inc (1990).

[62] N. Xing, H. Li, J. Dong, R. Long, and C. Zhang, Computational Materials Science **42**, 600 (2008).

VITA

Graduate School

Southern Illinois University

Said A. Bakkar

Bakkarsaeed@gmail.com

Yarmouk University, Jordan

Bachelor of Physics, January,1995

Al-Albayt University, Mafraq

Master of Science, Physics, March, 2000

Awards

Valedictorian, Al-al-Bayt University, Mafraq, Jordan, August 2000.

Thesis Title: NEW INVERSE-HEUSLER MATERIALS WITH POTENTIAL SPINTRONICS APPLICATIONS

Major Professor: Dr. Dipanjan Mazumdar

Publications

M. M. El-Hilo, A. L. Al-Momnee, and S. A. Bakkar, *Minor hysteresis loop phenomena in particulate recording media*, , Journal of Appl. Phys. Vol. 91, No 10,8742-8744, (2002).